

Open-system Evolution of a Crustal-scale Magma Column, Klamath Mountains, California

Calvin G. Barnes ^{1*}, Nolwenn Coint ², Melanie A. Barnes¹,
Kevin R. Chamberlain³, John M. Cottle⁴, O. Tapani Rämö⁵,
Ariel Strickland⁶ and John W. Valley⁷

¹Department of Geosciences, Texas Tech University, Lubbock, TX 79409-1053, USA; ²Norwegian Geological Survey, Trondheim 7491, Norway; ³Department of Geology and Geophysics, University of Wyoming, Laramie, WY 82071, USA; ⁴Department of Earth Science, University of California, Santa Barbara, Santa Barbara, CA 93106-9630, USA; ⁵Department of Geosciences and Geography, University of Helsinki, Helsinki FI-00014, Finland; ⁶Department of Geology, Lone Star College System, The Woodlands, TX 77381, USA; ⁷Department of Geoscience, University of Wisconsin, Madison, WI 53706-1692, USA

*Corresponding author. Telephone: 806 8347389. Fax: 806 7420100. E-mail: cal.barnes@ttu.edu

Received 3 February 2021; Accepted 21 July 2021

ABSTRACT

This study addresses the question of how and where arc magmas obtain their chemical and isotopic characteristics. The Wooley Creek batholith and Slinkard pluton are a tilted, mid- to upper-crustal part of a vertically extensive, late-Jurassic, arc-related magmatic system in the Klamath Mountains, northern California. The main stage of the system is divided into an older lower zone (c. 159 Ma) emplaced as multiple sheet-like bodies, a younger upper zone (c. 158–156 Ma), which is gradationally zoned upward from mafic tonalite to granite, and a complex central zone, which represents the transition between the lower and upper zones. Xenoliths are common and locally abundant in the lower and central zones and preserve a ghost stratigraphy of the three host terranes. Bulk-rock Nd isotope data along with ages and Hf and oxygen isotope data on zircons were used to assess the location and timing of differentiation and assimilation. Xenoliths display a wide range of ϵ_{Nd} (whole-rock) and ϵ_{Hf} (zircon), ranges that correlate with rocks in the host terranes. Among individual pluton samples, zircon Hf and oxygen isotope data display ranges too large to represent uniform magma compositions, and very few data are consistent with uncontaminated mantle-derived magma. In addition, zoning of Zr and Hf in augite and hornblende indicates that zircon crystallized at temperatures near or below 800 °C; these temperatures are lower than emplacement temperatures. Therefore, the diversity of zircon isotope compositions reflects *in situ* crystallization from heterogeneous magmas. On the basis of these and published data, the system is interpreted to reflect initial MASH-zone differentiation, which resulted in elevated $\delta^{18}O$ and lowered ϵ_{Hf} in the magmas prior to zircon crystallization. Further differentiation, and particularly assimilation–fractional crystallization, occurred at the level of emplacement on a piecemeal (local) basis as individual magma batches interacted with partial melts from host-rock xenoliths. This piecemeal assimilation was accompanied by zircon crystallization, resulting in the heterogeneous isotopic signatures. Magmatism ended with late-stage emplacement of isotopically evolved granitic magmas (c. 156 Ma) whose compositions primarily reflect reworking of the deep-crustal MASH environment.

Key words: crustal magma column; assimilation; zircon; geochronology

INTRODUCTION

Debate exists among workers who study the evolution of arc magmas: where and how do magmas obtain their chemical and isotopic characteristics? In addition to partial melting of variably metasomatized mantle wedge to produce basaltic and high-Mg andesitic magmas, many workers call on deep crustal hybridization (MASH or hot-zone processes) as a principal cause of chemical and isotopic diversity (e.g. Hildreth & Moorbath, 1988; Annen *et al.*, 2006; Schmidt & Grunder, 2011), whereas others invoke crystal-differentiation over much of the crustal column (see review by Jagoutz & Klein, 2018). Still other workers suggest that, depending on the plumbing system, magmas may undergo differentiation in middle- and upper-crustal reservoirs via crystal fractionation, mixing, and crustal assimilation (Humphreys *et al.*, 2006, 2009; Singer *et al.*, 2011; Ruprecht *et al.*, 2012; Spera & Bohrsen, 2018; many others). There thus remains considerable debate concerning the vertical dimensions of magma interconnectivity in arc systems, the longevity of such systems, the time and length scales of intra-crustal reservoirs, and the efficacy of petrological processes in each stage of magma transport and differentiation.

A common problem in addressing the depths of magmatic processes is the fact that many arc plutons are exposed over a small range of paleodepths. However, some plutonic systems are exposed in tilted crustal sections, permitting detailed study across many kilometers of original vertical extent [e.g. North Cascades (Matzel *et al.*, 2006, Gordon *et al.*, 2017); southern Sierra Nevada (Pickett & Saleeby, 1993, 1994; Klein & Jagoutz, 2021; Klein *et al.*, 2021); Kohistan (Jagoutz *et al.*, 2007, 2009); Sesia (Sinigoi *et al.*, 2016; Karakas *et al.*, 2019); Famatinian arc (Otamendi *et al.*, 2009, 2012; Tibaldi *et al.*, 2013; Walker *et al.*, 2015)]. One such example is the Wooley Creek batholith (WCB) and Slinkard pluton (SP) (Fig. 1), which together are a composite plutonic sequence in the Klamath Mountain province of northern California (Barnes *et al.*, 1986a). Post-magmatic tilting and erosion have exposed c. 15 km of structural relief in this plutonic system (Barnes *et al.*, 1986b; Coint *et al.*, 2013b). Moreover, adjacent high-grade host rocks are exposed through an additional c. 5–10 km of structural relief (Garlick *et al.*, 2009). Because of this structural relief, we can demonstrate that in the middle crust, magma emplacement traversed three distinct, stacked tectonostratigraphic terranes (Fig. 1; Coint *et al.*, 2013b).

Field and petrological study of the WCB–SP system (Barnes, 1983; Barnes *et al.*, 1986a, 1990, 1992, 2016a; Coint *et al.*, 2013a, 2013b) recognized the following: (1) the system is zoned, with mafic and intermediate rocks in the deepest, northeastern, structural levels, and intermediate to felsic rocks at higher, southern and southwestern levels (Fig. 1); (2) the oldest rocks in the system crop out in the lower, more mafic zone, with a broad decrease in ages into the upper felsic zone; (3) upper and

lower zones are separated by a central transition zone, which contains rocks with both old and young ages; (4) lower- and central-zone magmas were emplaced in relatively small batches, as exemplified by individual sheet-like intrusive units and corresponding variation in composition and texture; (5) magma mingling was widespread; (6) many rocks are cumulate in nature, with initial magma compositions that ranged from basaltic to dacitic; (7) bulk-rock Sr, Nd, and oxygen isotopes indicate that parental magmas were mixtures of mantle- and crust-derived components.

Xenoliths of varying lithology and degrees of partial melting and digestion are locally abundant in the system, which initially led to the interpretation that the crustal isotopic components in these plutons were the result of *in situ* assimilation (Barnes *et al.*, 1987). However, later bulk-rock oxygen isotope data suggested that interaction with crustal rocks also occurred below the level of emplacement by interaction with deep-seated metasedimentary rocks (Barnes *et al.*, 1990).

This paper presents new age and geochemical data on zircon from the WCB–SP, xenoliths, and wall rocks, plus bulk-rock Nd isotope compositions on xenoliths, their plutonic hosts, and probable cognate host rocks. These data are integrated with published trace element compositions of clinopyroxene and amphibole to assess conditions of zircon stability. The combined data indicate that the WCB–SP is the exposed part of a crustal-scale magma column in which magma compositions evolved over a time interval of c. 4 Myr. Hybridization with crustal rocks and/or magmas occurred both in the lower crust and at the level of emplacement, where a ghost stratigraphy of partially melted xenoliths is preserved. Emplacement-level assimilation resulted in isotopic heterogeneity at the hand sample, outcrop, and pluton scale.

GEOLOGICAL SETTING

The WCB–SP is a Late Jurassic plutonic complex in the Klamath Mountain accretionary province of northern California (Irwin, 1972, 1981; Snoko & Barnes, 2006). The complex intrudes three tectonostratigraphic terranes (Fig. 1) that were amalgamated during the c. 170 Ma Middle Jurassic Siskiyou orogeny (Coleman *et al.*, 1988; Barnes *et al.*, 2006; Barnes & Barnes, 2020). In ascending structural order, the terranes are: (1) the Rattlesnake Creek terrane (RCT), an ophiolitic mélange overlain by a cover sequence of metavolcanic and metasedimentary rocks (Gray, 1986; Wright & Wyld, 1994; Frost *et al.*, 2006); (2) the western Hayfork terrane (wHt), a Middle Jurassic, metamorphosed, volcanogenic, crystal-lithic arenite with intercalated argillite and lahar deposits (Wright & Fahan, 1988; Hacker *et al.*, 1995; Donato *et al.*, 1996; Barnes & Barnes, 2020), which is in faulted depositional contact with the underlying Rattlesnake Creek terrane (Wright & Fahan, 1988; Donato *et al.*, 1996); (3) the eastern Hayfork terrane

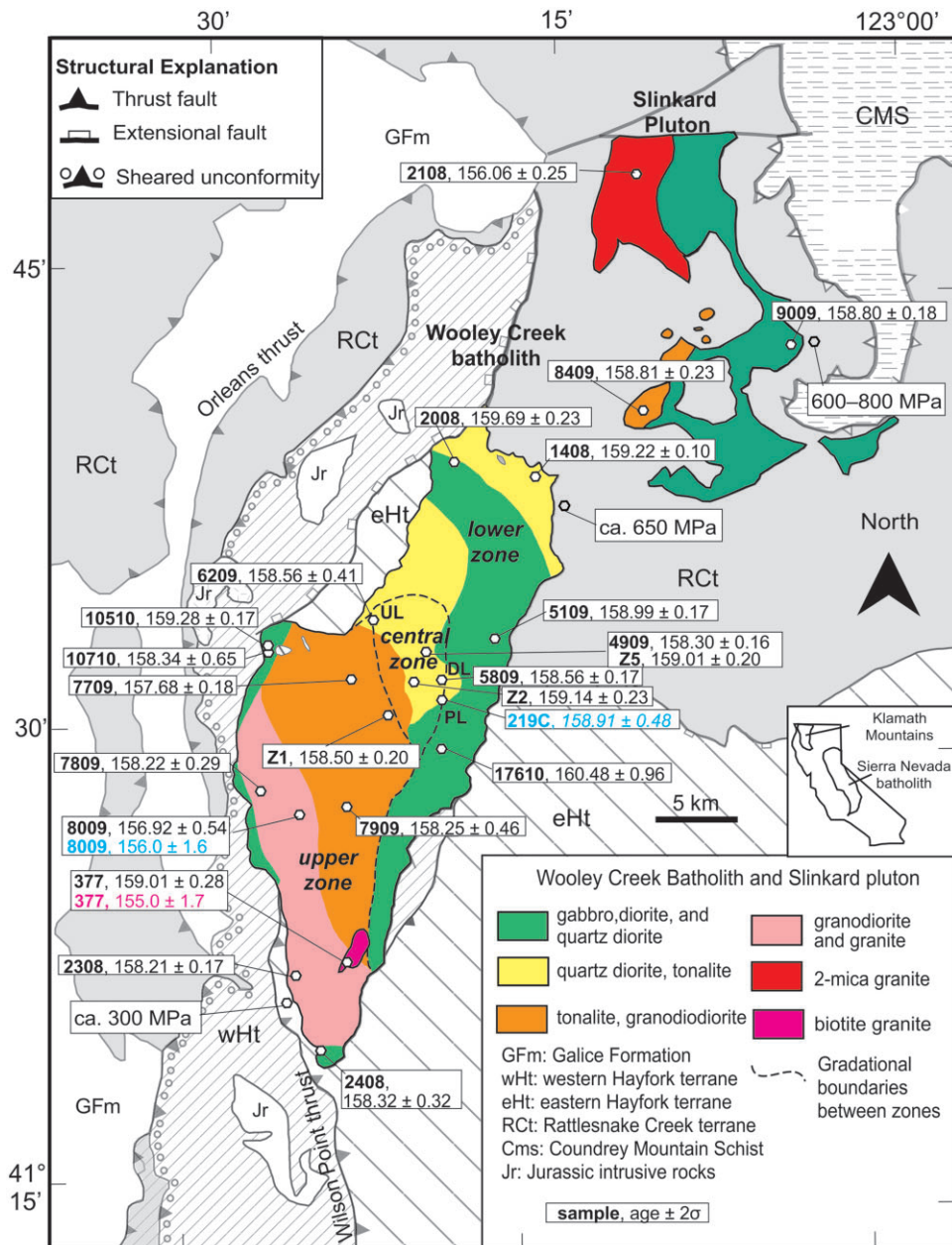


Fig. 1. Simplified geological map of the Wooley Creek batholith–Slinkard pluton intrusive complex (modified from [Wagner & Saucedo, 1987](#), and [Barnes, 1987](#)) with the locations and ages of dated samples. Ages in black text were determined by CA-ID-TIMS, those shown in red text by SHRIMP-RG, and those shown in blue text by LA-ICP-MS. The lower zone encompasses the lower Wooley Creek batholith and the Slinkard pluton, except for the two-mica granite. Except for samples Z1, Z2, Z5, 377, and 219C, all sample numbers have the prefix WCB. Samples 377 and 219C have the prefix MMB. DL, Deadman Lake; UL, Ukonom Lake; PL, Pleasant Lake.

(eHt), a chert–argillite mélange and broken formation composed mainly of metamorphosed chert, argillite, and quartzose wackes, with Proterozoic to Triassic blocks of ribbon chert, quartzite, marble, peridotite, metabasic rocks, and rare blueschist ([Irwin, 1972](#); [Wright, 1982](#); [Ernst, 1990, 1998](#); [Ernst et al., 2008, 2017](#)). Intergranular calcite is common in the chert–argillite mélange rocks of the eHt. The eHt overlies the wHt along the Wilson Point thrust ([Wright, 1982](#); [Barnes et al., 2006](#)).

Post-amalgamation regional metamorphism affected all three terranes, with metamorphic grade increasing from greenschist facies in the southern part of the area to granulite facies in the north–central part (e.g. [Coleman et al., 1988](#); [Donato, 1989](#); [Ernst, 1999](#); [Garlick et al., 2009](#)). Emplacement of the WCB–SP was originally interpreted to post-date peak metamorphism ([Barnes, 1983](#)). However, recent work suggests that regional metamorphism was continuing during WCB–SP magmatism ([Dailey et al., 2019](#)). During the Nevadan

orogeny, the WCB–SP and host terranes were thrust westward (modern coordinates) over outboard terranes of the Western Jurassic belt (Fig. 1; Lanphere *et al.*, 1968; Irwin, 1972; Jachens *et al.*, 1986; Snoke & Barnes, 2006). Subsequent regional doming was centered on the present outcrop area of the Condrey Mountain Schist (Fig. 1; Mortimer & Coleman, 1985), tilting the overlying terranes and plutons, so that erosion has exposed significant structural relief in the complex (Barnes *et al.*, 1986b). For example, on the basis of contact metamorphic mineral assemblages, the estimated pressure near the structurally highest (southwestern) part of the WCB was *c.* 300 MPa, which is consistent with the transition from andalusite to sillimanite in the aureole (Barnes *et al.*, 1986b). Contact metamorphic pressure at the NE contact of the WCB was estimated at 650 MPa on the basis of GASP assemblages in semipelitic rocks and the olivine–orthopyroxene assemblage in metaserpentinite (Barnes *et al.*, 1986b). Thermobarometric modeling of migmatitic, rutile-bearing garnet amphibolites exposed at the base of the SP yielded a pressure range of *c.* 600–800 MPa (Leib *et al.*, 2020). Thus, a conservative pressure difference across the intrusive complex yields *c.* 11 km of structural relief, whereas use of the maximum pressure estimate at the base of the SP leads to calculated structural relief of *c.* 18 km, all using measured densities of the host rocks (Jachens *et al.* 1986).

WCB–SP intrusive complex

The WCB–SP ranges from gabbroic to granitic rocks, which are magnesian and calcic according to the Frost *et al.* (2001) classification. Except for mildly peraluminous late-stage granitic bodies, the rocks are metaluminous. Detailed discussion of bulk-rock major, trace, and isotopic compositions have been presented by Barnes *et al.* (1986a, 1990, 2016a) and Coint *et al.* (2013a, 2013b). On the basis of rock type, bulk-rock chemical compositions, cross-cutting relationships, and U–Pb (zircon) age data, the complex was divided into main (or early) and late stages (Fig. 1; Coint *et al.*, 2013b). The voluminous main stage consists of three zones. The lower zone includes the lower WCB and gabbroic to tonalitic parts of the SP. It was emplaced as a series of sheet-like bodies whose individual thicknesses varied from a few centimeters to tens of meters. Some intrusive sheets mixed with pre-existing magmas, whereas others represent distinct intrusive units (Coint *et al.*, 2013a). Synplutonic mafic dikes in various stages of disruption are widespread in the lower zone (Coint *et al.*, 2013b; Barnes *et al.*, 2016a). Chemical abrasion isotope dilution thermal ionization mass spectrometry (CA-ID-TIMS) U–Pb (zircon) analysis yielded weighted average ages of 159.69 ± 0.23 to 158.81 ± 0.23 Ma (all uncertainties cited are 2σ ; Coint *et al.*, 2013b; this work). Xenoliths are widespread and locally abundant; they are described in more detail below.

The upper zone consists of the upper part of the WCB, which is crudely zoned from structurally lower tonalite to structurally higher granodiorite and granite (Fig. 1; Coint *et al.*, 2013b; Barnes *et al.*, 2016a). This upward zonation is expressed as a decrease in mafic minerals and an increase in quartz and alkali-feldspar (Barnes, 1983; Coint *et al.*, 2013b). Unlike the lower zone, individual sheet-like intrusions are absent. Instead, dense swarms and pillowed zones of mafic magmatic enclaves are present in basal parts of the upper zone; these give way to dispersed enclaves in structurally higher parts of the zone. Chemical abrasion-ID-TIMS U–Pb (zircon) dating yielded ages predominantly from 158.21 ± 0.17 to 157.68 ± 0.18 Ma (Coint *et al.*, 2013b; this work). In addition, one granitic sample that is texturally identical to the rest of the upper zone yielded a single-crystal ID-TIMS (zircon) age of 156.92 ± 0.54 Ma (this work, see discussion below). Xenoliths are uncommon in the upper zone except near intrusive contacts.

The upper and lower zones are locally separated by the transitional central zone (Fig. 1), which is a plexus of sheet-like bodies that range in width from 1 to 10 m, in composition from gabbro to tonalite, and in shape from planar sheets to intensely deformed (folded, boudinaged, disrupted) synplutonic dikes (Barnes *et al.*, 1986a; Coint *et al.*, 2013b). Five samples yielded CA-ID-TIMS (zircon) ages of 159.14 ± 0.23 , 159.01 ± 0.20 , 158.65 ± 0.41 , 158.56 ± 0.17 , and 158.30 ± 0.16 Ma (Coint *et al.*, 2013b; this work). These data indicate that the central zone formed over a prolonged interval that encompassed both upper- and lower-zone ages. Xenoliths are locally abundant in the central zone, particularly in the transition between central- and lower-zone rocks.

Mafic selvages (mainly diorite and quartz diorite) are exposed along parts of the western and southern contacts of the upper zone (Fig. 1). Two samples from the largest western selvage were dated to 159.28 ± 0.17 and 158.34 ± 0.65 Ma, spanning lower- and upper-zone ages, whereas the southern selvage yielded an age of 158.32 ± 0.32 Ma, equivalent to upper-zone ages (Coint *et al.*, 2013b; this work).

Late-stage magmatism in the WCB–SP consists of two granitic bodies (Fig. 1). The NW side of the SP is underlain by a garnet-bearing two-mica granite with a CA-ID-TIMS (zircon) age of 156.0 ± 0.06 Ma (this work). A smaller hornblende-bearing biotite granite intrudes the upper zone of the WCB; zircon from this sample yielded a sensitive high-resolution ion microprobe-reverse geometry (SHRIMP-RG) age of 155.0 ± 1.7 Ma (this work).

Xenoliths

Xenoliths vary widely in distribution, rock type, size, and shape. Xenoliths are common and locally abundant along intrusive contacts, particularly along the eastern contact and within selvages in the west and south (Fig. 2). Xenoliths are widespread throughout the lower

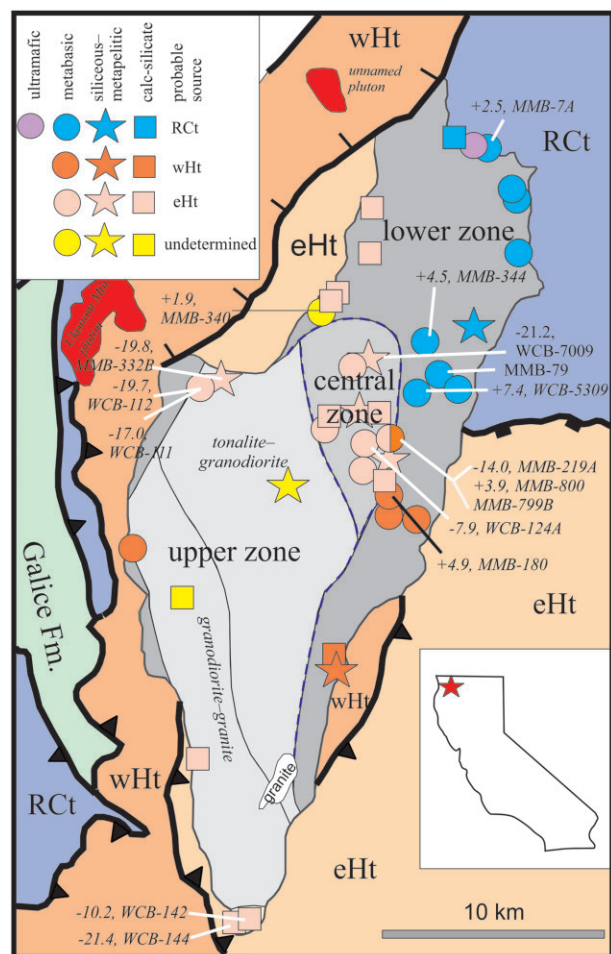


Fig. 2. Simplified geological map of the Wooley Creek batholith illustrating the distribution of xenoliths and their interpreted relationships to the host metamorphic terranes. Labeled sample locations indicate the bulk-rock ϵ_{Nd} (158 Ma) and the sample number. The thin black line in the upper zone separates structurally lower tonalitic to granodioritic rocks from structurally higher granodioritic to granitic rocks. The extensional fault that cuts the NW side of the pluton is a high-angle normal fault; the extensional fault east of the pluton is low angle.

zone and in the transition between lower and central zones, where they range in shape from elongate, screen-like bodies to isolated, rounded to angular masses a few centimeters in length (Fig. 3). Screen-like bodies reach as much as 100 m in length and 20 m in width.

Xenolith rock types vary from peridotite to quartz-rich meta-arenite (Fig. 2), with all but the most refractory (e.g. peridotite, skarn) showing textural evidence of partial melting. Peridotite is metamorphosed to $\text{Ol} + \text{Opx}$ assemblages [mineral abbreviations from Whitney & Evans (2010)] and rare Fe-rich gabbroic xenoliths contain centimeter-scale garnet porphyroblasts. Many xenoliths, and particularly those in the lower and central zones and western selva, are gneissic, display granoblastic textures, and contain prograde $\text{Cpx} + \text{Pl} \pm \text{Opx} \pm \text{Amp} \pm \text{Bt} \pm \text{Qz}$ (Fig. 4). These latter xenolith types are migmatitic, with layer-parallel and cross-cutting

leucosomes (Fig. 3a–c), which in many cases coalesce (Fig. 3b and c). Although the majority of migmatitic xenoliths are characterized by $\text{Aug} \pm \text{Opx} \pm \text{Amp} + \text{Plag}$ assemblages, a few contain sillimanite \pm cordierite \pm $\text{Bt} \pm \text{Opx}$ (Fig. 4b). These pelitic to semipelitic xenoliths are typically mafic, with large proportions of Opx and Bt.

In thin section, migmatitic xenoliths and some quartz-rich meta-arenite xenoliths display thin films and re-entrants of quartz and feldspars: textural evidence for the presence of an intergranular melt (Fig. 4; e.g. Sawyer, 1999; Holness & Sawyer, 2008). Some xenoliths are composite (Fig. 3d), in which granofels xenoliths were engulfed by a quartz gabbroic magma, which was then disrupted by a later gabbroic magma. Such examples illustrate the temporal development of the lower and central zones via episodic magma emplacement, accompanied by disruption of, and mingling with older plutonic material and xenoliths.

Above the lower- to central-zone transition, large screen-like bodies are lacking, and with increasing structural height xenoliths become less abundant and smaller, generally no more than 30 cm in diameter. Rock types range from migmatite to calc-silicate skarn, quartz-rich meta-arenite (Fig. 3e) and amphibolite (Fig. 3f). In the upper zone, xenoliths are less common and are predominantly calc-silicates and metaquartzite. The metaquartzitic xenoliths display textural evidence such as pseudomorphosed melt films and re-entrants indicative of partial melting (see Holness & Sawyer, 2008).

The diversity of xenoliths and of host-rock lithologies would suggest that it should be possible to correlate xenoliths with their source host-rock terranes. Such distinctions are possible in the case of peridotite, amphibolite, and quartz-rich meta-arenite, with the first two correlative to the RCt and the third to the eHt. However, apart from xenoliths sampled in contact zones, metamorphism and partial melting obscured diagnostic lithological and textural relationships. Therefore, correlation of xenoliths with potential host-rock lithologies utilized age and geochemical features, as presented in the Results and Discussion sections.

ANALYTICAL METHODS

Sample preparation

Bulk-rock samples were crushed in steel jaw mills and powdered in an alumina shatterbox. These powders were used for major and trace element analysis (Coit et al., 2013b; Barnes et al., 2016a) and Nd isotope analysis (this work). Zircon was separated by traditional heavy liquid and magnetic processes at Texas Tech or the University of Wyoming. Hand-picked crystals were embedded in 25 mm-diameter epoxy rounds. Prior to oxygen isotope analysis, KIM-5 oxygen isotope standard (Valley, 2003, $\delta^{18}\text{O} = 5.09\text{‰}$ VSMOW) was added to the mount, and the mount was re-polished, taking extra

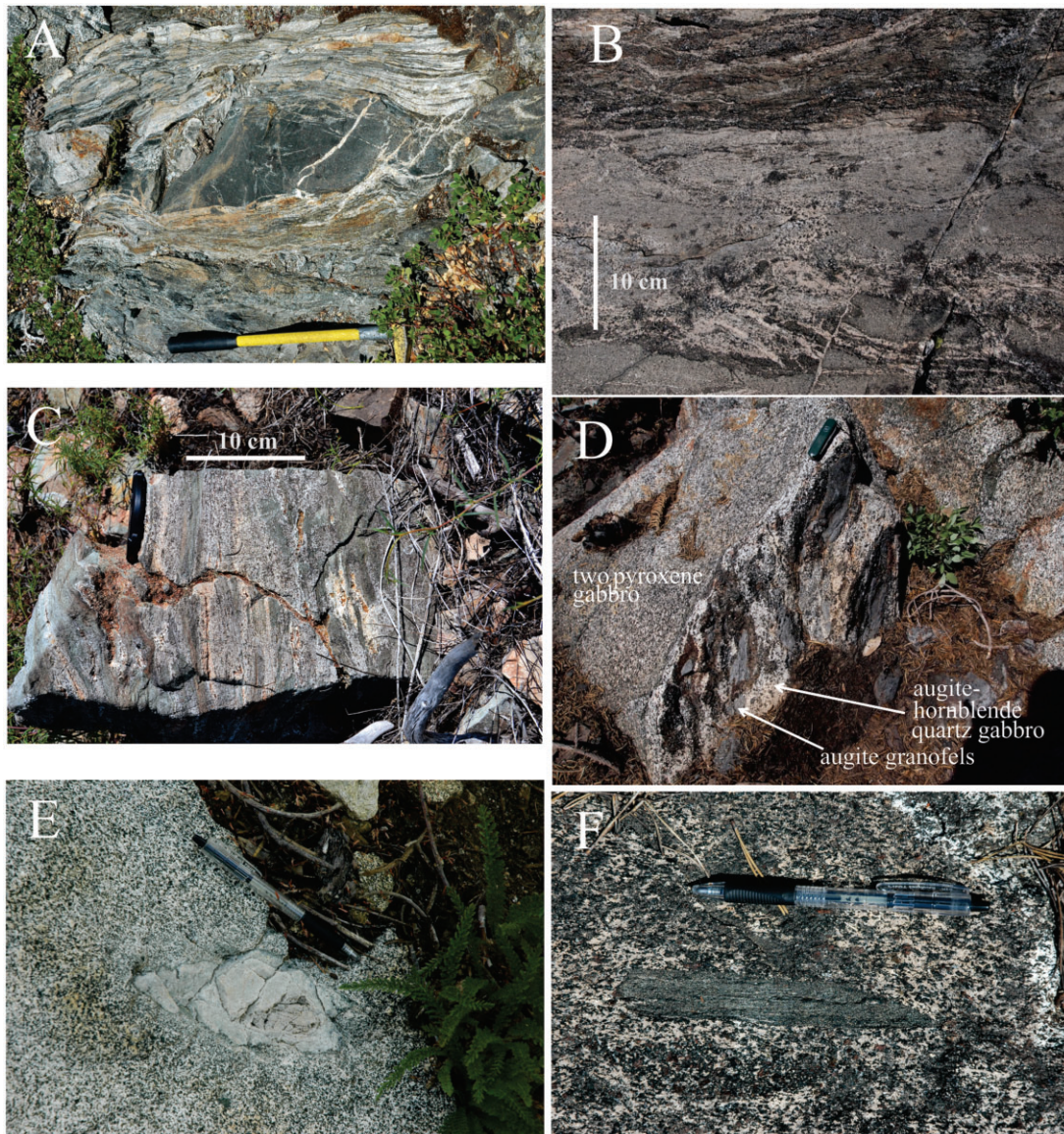


Fig. 3. Photographs of xenoliths in the lower and central zones. (a) Migmatitic semipelitic xenolith cut by a mafic syn-plutonic dike; Pleasant Lake basin (central- to lower-zone transition; Fig. 1). The dike is boudinaged in the xenolith and cut by leucosome veins derived from the xenolith. (b) Migmatitic metasedimentary screen; Pleasant Lake basin, showing compositional layering and anastomosing leucosomes. (c) Migmatitic xenolith of eastern Hayfork terrane protolith; western contact near lower- to central-zone transition. (d) A composite xenolith composed of fine-grained augite granofels brecciated by augite-hornblende quartz gabbro, all enclosed in two-pyroxene gabbro; NW of Pleasant Lake. The knife is 6 cm long. (e) Siliceous xenolith in quartz diorite, central zone. (f) Amphibolitic xenolith in quartz diorite, central zone. The pen is 15 cm long.

care to achieve a smooth, flat, low-relief polish. Zircon mounts were gold coated prior to SHRIMP-RG and oxygen isotope analysis; these coatings were removed before Hf isotope analysis.

In addition to zircon age data determined by CA-ID-TIMS, a total of 498 grains from the WCB-SP were analyzed, 232 by SHRIMP-RG and 266 by laser ablation multicollector inductively coupled plasma mass spectrometry (LA-MC-ICP-MS). The LA-MC-ICP-MS system was also used to analyze Hf isotope ratios. These methods were also used to determine ages of xenolith zircons (68 by SHRIMP-RG and 24 by LA-MC-ICP-MS) and

wall-rock zircons (28 by SHRIMP-RG and 48 by LA-MC-ICP-MS).

CA-ID-TIMS

Chemical abrasion ID-TIMS dating was done at the University of Wyoming. Zircon crystals were picked based on the cathodoluminescence (CL) images. Both elongated grains (150–200 μm), unlikely to contain inherited cores, and more equant zircons were selected in an attempt to obtain ages from distinct zircon populations and date stages of crystallization. Zircons were

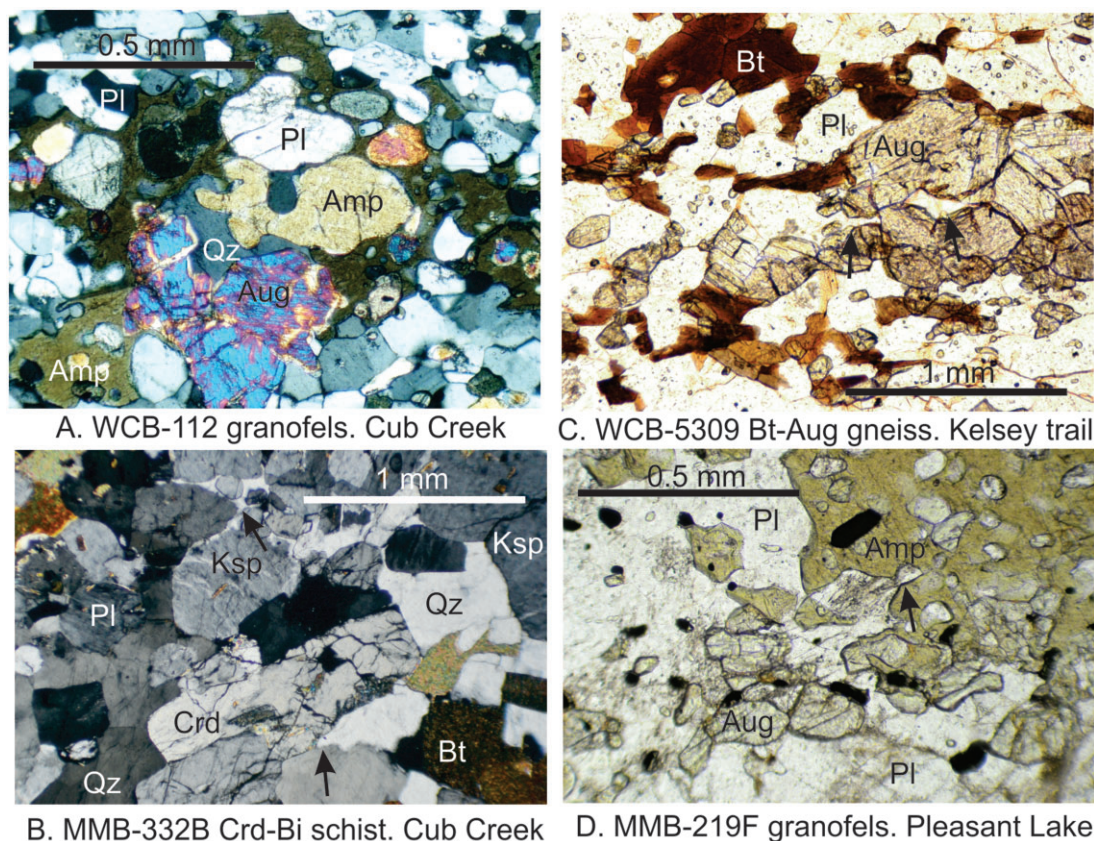


Fig. 4. Photomicrographs of xenoliths. Poikilitic habits, thin re-entrants, and small dihedral angles (black arrows) all indicate that the xenoliths underwent partial melting after incorporation into the WCB. Samples illustrated in (a) and (b) have eastern Hayfork terrane protoliths and were sampled at locations J and K (Fig. 2). Sample WCB-5309 (c) has a probable Rattlesnake Creek terrane protolith and was sampled at location E (Fig. 2). Sample MMB-219F has an eastern Hayfork terrane protolith and was sampled at location G (Fig. 2). Mineral abbreviations from Whitney & Evans (2010).

annealed and chemically abraded to remove damaged parts of the crystals and reduce discordance (Mattinson, 2005). Details of the dissolution of zircon grains and the analytical procedure have been given by Anderson *et al.* (2013).

Secondary ion mass spectrometry (SIMS)

Oxygen isotope analysis was performed at the University of Wisconsin WiscSIMS laboratory using a CAMECA IMS-1280 ion microprobe following the procedures outlined by Kita *et al.* (2009) and Valley & Kita (2009). A focused, 10 kV Cs⁺ primary beam was used for analysis at 1.9–2.2 nA and a corresponding spot size of 10–15 μm. A normal incident electron gun was used for charge compensation. The secondary ion acceleration voltage was set at 10 kV and ¹⁶O, ¹H¹⁶O and ¹⁸O were collected in three Faraday cups simultaneously. Values of OH/O were corrected for background (Wang *et al.*, 2014). Four consecutive measurements of zircon standard KIM-5 were made at the beginning and end of each session, and after every 10–20 unknowns throughout each session. The average values of the standard analyses that bracket each set of unknowns were used to correct for instrumental bias. The average precision (reproducibility) of the bracketing standards for this

study ranged from ±0.12 to ±0.34‰ and averaged ±0.19‰ (2 standard deviations).

SHRIMP-RG

Mounted zircon crystals were imaged by cathodoluminescence on the JEOL JSM 5600 scanning electron microprobe at the USGS/Stanford Microanalytical laboratory. The zircons were then analyzed for both U–Pb isotopes and rare earth elements (REE) on the SHRIMP-RG following the method described by Mazdab & Wooden (2006). Analyzed spots are about 20 μm in diameter and 1–2 μm deep.

Laser ablation ICP-MS

Zircon was analyzed by LA-MC-ICP-MS at the University of California, Santa Barbara in three sessions. In the first session, untreated and annealed, chemically abraded zircons from sample WCB-4909, and annealed, chemically abraded zircons from samples WCB-6209 and WCB-10510 were analyzed. Annealed, chemically abraded grains were analyzed in an attempt to explain unrealistically young ages determined by SHRIMP-RG, as discussed in the Results section. In this and the second session, U–Pb ages were determined first,

followed by analysis of Hf isotopes, all using a Photon Machines 193 nm excimer laser and Nu Instruments Plasma HR MC-ICP-MS system. In the third session, a subset of samples previously dated by SHRIMP-RG were analyzed for Hf isotopes and another set was analyzed by split-stream, with U–Pb data collected on the Nu Instruments ATToM single-collector ICP-MS system and Hf on the multicollector instrument.

Bulk-rock Nd isotope analysis

Whole-rock Sm–Nd ID-TIMS isotope analyses were performed at the Research Laboratory (Radiogenic Isotopes) of the Geological Survey of Finland. Approximately 150–250 mg fractions were spiked with a ^{149}Sm – ^{150}Nd tracer. Silicic (>65 wt% SiO_2) samples were dissolved, for a minimum of 48 h, in a Teflon bomb at 180 °C in a 1:4 mixture of HNO_3 , mafic (<65 wt% SiO_2) samples, for a minimum of 48 h, in Savillex® screw-cap Teflon beakers on a hot plate. After evaporation, the samples were dissolved in HCl to obtain a clear solution. The light rare earth elements (LREE) were separated using standard cation exchange chromatography. Sm and Nd were purified on quartz columns according to the method of Richard *et al.* (1976). The total procedural blank was $<0.00003 \mu\text{g g}^{-1}$ for Nd. Isotope ratios of Sm and Nd were measured using a VG Sector 54 multi-collector mass spectrometer (those of Nd in dynamic mode). The $^{143}\text{Nd}/^{144}\text{Nd}$ ratio was fractionation corrected for $^{146}\text{Nd}/^{144}\text{Nd} = 0.7219$ and repeated analyses of the La Jolla Nd standard gave $^{143}\text{Nd}/^{144}\text{Nd}$ of 0.511850 ± 0.000022 (mean and external 2σ error of 122 measurements). The external 2σ error on $^{143}\text{Nd}/^{144}\text{Nd}$ was thus 0.0035% and the Sm–Nd ratios are estimated to be accurate within 0.5%. The maximum error in the ϵ_{Nd} values is $\pm 0.4 \epsilon$ -units.

ZIRCON DESCRIPTIONS

Six samples from the main-stage lower zone were analyzed, along with a single sample from the late-stage two-mica granite of the SP (Fig. 1) and a sample collected adjacent to a metapelitic xenolith in the transition between lower- and central-zone rocks (MMB-219C). Zircon from lower-zone dioritic samples is relatively large (broken crystals vary from 300 to 600 μm long) and prismatic, with well-developed {101} and {110} forms displaying homogeneous cores surrounded by broad oscillatory-zoned mantles and rims (Fig. 5a, sample WCB-9009). Many zircon grains occur at boundaries between pyroxene and plagioclase, suggesting relatively late crystallization. Zircon from tonalitic samples (WCB-1408, 2008, 8409) is smaller and prismatic. Many crystals contain dark inclusions in transmitted light and in CL some display sector zoning in addition to oscillatory zoning (Fig. 5a).

Zircon from the SP two-mica granite occurs as inclusions in quartz, is locally associated with sillimanite (after biotite), and displays various habits and sizes. A

few crystals are prismatic, c. 250 μm long, have length-to-width ratios of c. 8:1, and display sharp concentric zoning in CL images (Fig. 5b). Other crystals are approximately equant, with {101} forms and pyramidal tips. CL imaging reveals homogeneous cores surrounded by concentric, oscillatory-zoned rims. Crystal lengths vary between 100 and 250 μm .

Four samples from the central zone were analyzed; they are Bt–Hbl quartz diorite and Bt–Hbl tonalite with relict pyroxene cores in hornblende. Zircon displays various morphologies and sizes and can be found as inclusions in Pl, Hbl, Bt, and Qz. Samples from the central zone contain two main zircon populations (Fig. 5c). The first is composed of prismatic grains 150–300 μm long, with well-developed {101} forms and length-to-width ratio of 2:1. The second population consists of equant crystals 70–150 μm in diameter that are concentrically zoned with thin, CL-bright rims (Fig. 5c). Some crystals have sector-zoned cores surrounded by oscillatory-zoned rims and in a few the core is truncated. One sample (WCB-6209) contains equant zircon from 100 to 200 μm in diameter with sector-zoned cores surrounded by a CL-bright ring and oscillatory-zoned darker rims.

Six upper-zone samples were analyzed (Fig. 1; samples Z1, 2308, 7709, 7809, 7909, and 8009); they vary from Bt–Hbl tonalite to Hbl–Bt granite. Zircon occurs as small inclusions in Hbl and Bt and as larger, prismatic to pyramidal grains along grain boundaries. As in the central zone, each of these samples contains two main zircon populations. One population is prismatic and elongate (100–200 μm), with length-to-width ratios of 3:1 to 5:1. These crystals tend to have darker cores and display relatively simple zoning patterns, except for a few crystals that have truncated cores surrounded by oscillatory-zoned rims. The other population is made of pyramidal to sub-equant crystals, <50 to 200 μm long, in which CL imaging reveals the presence of highly discordant core zones, generally darker in the image, surrounded by oscillatory-zoned lighter rims (Fig. 5d).

Two dioritic to quartz dioritic samples from the western mafic selvage were analyzed (WCB-105 and WCB-107). Both contain zircons similar to those found in lower-zone tonalitic rocks. The sample from the southern mafic selvage (WCB-2408) is a weakly porphyritic two-pyroxene diorite. Elongate prismatic zircon crystals occur as inclusions in anhedral hornblende and biotite, have moderately well-developed {101} forms, and display simple zoning patterns in CL images (Fig. 5e).

The late-stage Hbl-bearing Bt granite intrusion that intrudes the upper zone (MMB-377; Fig. 1) contains oscillatory-zoned zircon that occurs along feldspar–biotite–quartz grain boundaries and as inclusions in quartz. Zircon from this sample is divided into three groups: prismatic crystals with length-to-width ratio 2:1 to 4:1, pyramidal crystals (Fig. 5f), and equant crystals. Crystal lengths vary from 100 to 250 μm for prismatic and pyramidal populations, whereas equant crystals are >100 μm in diameter.

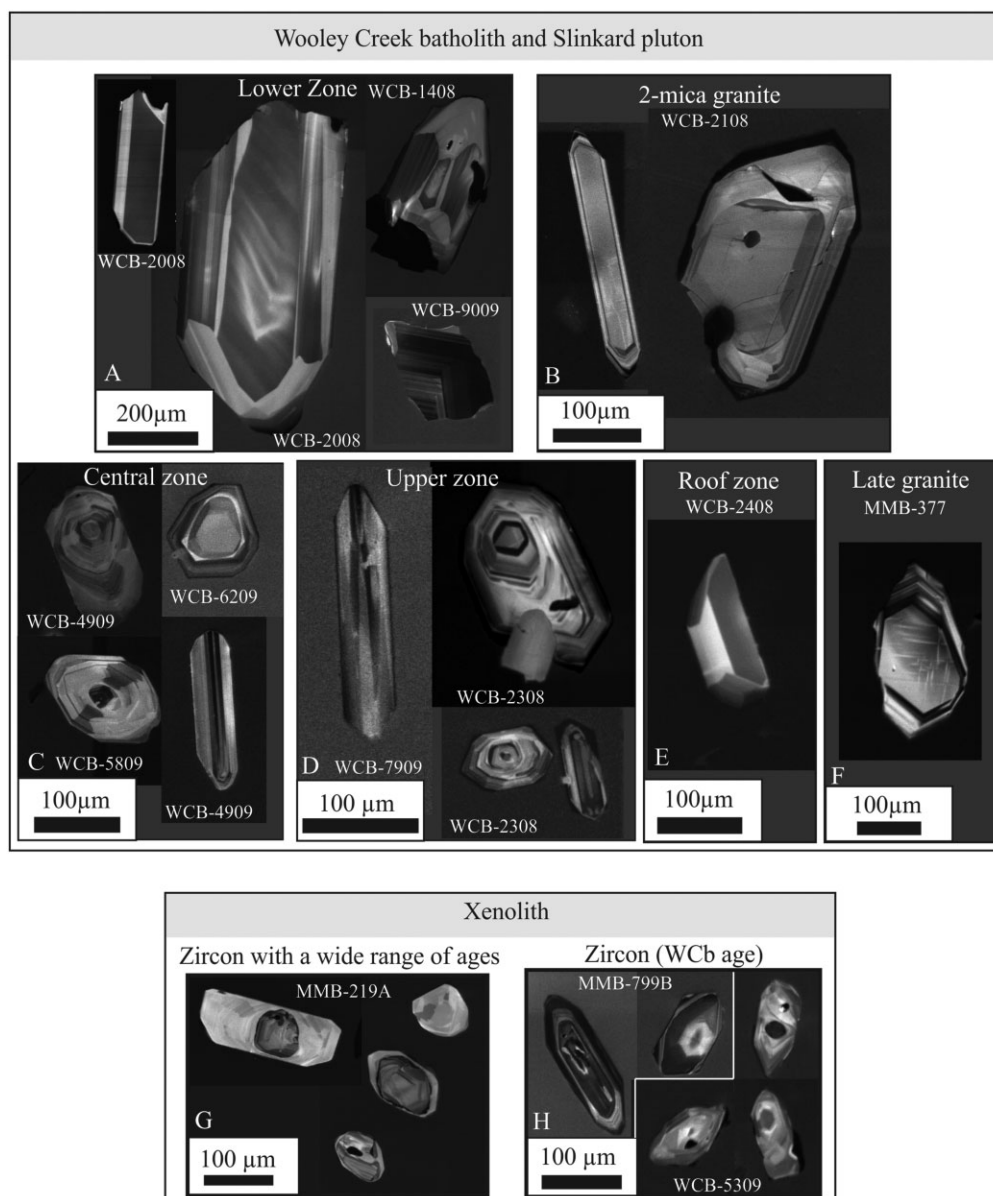


Fig. 5. Cathodoluminescence images of representative zircon crystals from each part of the WCB, SP and xenoliths. (a) Lower zone: WCB and mafic part of the Slinkard pluton. (b) Slinkard pluton, late-stage two-mica granite. (c) Central zone. (d) Upper zone. The truncated oscillatory-zoned cores should be noted. (e) Southern selvage or 'roof zone'. (f) Southern late-stage biotite granite. (g) Detrital zircon in metasedimentary xenolith from Pleasant Lake (Fig. 2). (h) Xenolith zircons that yielded U–Pb ages similar to the age of the WCB.

Zircons from xenoliths MMB-219A and WCB-7009 are widely variable in habit and zoning (Fig. 5g), consistent with their origin as detrital grains in the original sedimentary protolith (see below). In contrast, zircons from xenoliths MMB-799B and WCB-5309 are prismatic to pyramidal, oscillatory zoned, and commonly display distinct core zones (Fig. 5h).

RESULTS

Results of CA-ID-TIMS dating are presented in Table 1. Complete data files for LA-ICP-MS analyses (U–Pb, Hf), SHRIMP-RG U–Pb analyses, and SIMS oxygen isotope analyses, along with sample map and sample locations,

are available in the Dryad Digital Repository, at <https://doi.org/10.5061/dryad.pvmcvdnk2>. A summary of oxygen isotope results is presented in Table 2 and Nd isotope data are given in Table 3. A summary of U–Pb ages determined by all three methods is presented in Supplementary Data File 1; supplementary data are available for downloading at <http://www.petrology.oxfordjournals.org>.

U–Pb ages

Plutonic rocks

All CA-ID-TIMS U–Pb ages are plotted in Fig. 6a, and all U–Pb dating results are plotted in Fig. 6b. U–Pb ages

Table 1: CA-TIMS U–Pb zircon data

Sample	Weight U (μg)	Pb (ppm)	Sample cPb (pg)	Pb*/Pbc (pg)	Th/U	Corrected atomic ratios				206/238 Th date (Ma)	err	207/235 date (Ma)	207/206 Th date (Ma)	Rho	Run date				
						²⁰⁶ Pb/ ²⁰⁴ Pb	²⁰⁸ Pb/ ²⁰⁶ Pb	²⁰⁸ Pb/ ²³⁸ U	²⁰⁷ Pb/ ²³⁵ U										
Upper zone																			
WCB Z1 (Bi Hb tonalite) 41-52513454, -123-3536114; 158.5 ± 0.2 Ma single grain, or inheritance trend with Z2, 157.8 ± 0.7 Ma																			
eq eu sA	2-52	580	19.9	50.1	13.6	2.8	0.41	193	0.14	0.02570 (0.7)	0.1886	(2.9)	0.0532 (2.6)	163.61	±1.18	175.4	338.0	0.43	2012
el sA	3-38	389	10.0	33.9	2.3	14.9	0.46	930	0.15	0.02489 (0.1)	0.1701	(1.1)	0.0496 (1.0)	158.46	±0.20	159.5	175.6	0.37	2012
WCB7709 (Bi Hb tonalite) 41-5301633, -123-37826; 157.68 ± 0.18, 2σ, MSWD 1.2, 2 points, 2 antecrystic																			
sA	3-40	256	6.9	23.6	4.3	5.0	0.32	336	0.10	0.02475 (0.2)	0.1669	(1.9)	0.0489 (1.8)	157.59	±0.25	156.7	143.1	0.51	2012
sB	2-59	121	3.4	8.8	2.6	3.1	0.51	207	0.16	0.02496 (0.2)	0.1697	(4.4)	0.0493 (4.2)	158.91	±0.31	159.2	162.8	0.72	2012
sC	11-25	142	3.6	40.1	2.6	15.5	0.35	1000	0.11	0.02478 (0.2)	0.1664	(1.0)	0.0487 (1.0)	157.79	±0.26	156.3	134.0	0.35	2012
sE	1-58	383	11.7	18.4	4.6	3.2	0.30	225	0.10	0.02491 (0.3)	0.1682	(2.1)	0.0490 (2.0)	158.64	±0.51	157.9	146.4	0.26	2017
Central zone																			
WCB Z2 (Bi Hb quartz diorite) 41-53688069, -123-3445404; 159.14 ± 0.23 Ma weighted mean 6/8, 2 points, MSWD 1.5; or inheritance trend with Z1																			
sA	5-06	129	3.2	16.4	1.3	12.6	0.35	815	0.11	0.02510 (0.1)	0.1748	(1.3)	0.0505 (1.3)	159.82	±0.22	163.6	218.8	0.41	2012
sB	16-80	91	2.4	39.8	3.6	10.5	0.31	692	0.10	0.02506 (0.5)	0.1741	(2.1)	0.0504 (1.9)	159.57	±0.73	163.0	212.7	0.41	2012
sC	8-60	127	3.2	27.4	1.5	17.8	0.37	1136	0.12	0.02499 (0.2)	0.1731	(1.0)	0.0502 (1.0)	159.09	±0.24	162.1	205.7	0.37	2012
WCB5809 (Hb Bi leucodiorite) 41-54007617, -123-3171031; 158.56 ± 0.17 Ma weighted mean 6/8, 4 points, MSWD 0.93, 1 antecrystic, X/Y/Z uncertainties ± 0.17/0.18/0.24 Ma																			
sC	2-70	164	4.1	11.1	1.3	8.1	0.27	546	0.08	0.02488 (0.2)	0.1671	(1.7)	0.0487 (1.7)	158.43	±0.28	156.9	133.5	0.42	2017
sD	6-48	157	4.2	27.1	1.4	18.7	0.61	1128	0.19	0.02470 (0.3)	0.1653	(1.1)	0.0485 (1.0)	157.30	±0.45	155.3	125.7	0.39	2017
sE	6-75	60	1.6	10.5	1.5	6.6	0.32	442	0.10	0.02493 (0.2)	0.1697	(1.6)	0.0494 (1.5)	158.73	±0.34	159.2	166.2	0.43	2020
sF-2g	3-38	53	1.3	4.5	0.5	9.9	0.40	639	0.13	0.02498 (0.2)	0.1702	(1.5)	0.0494 (1.5)	159.08	±0.32	159.6	167.1	0.42	2020
sG	3-60	84	2.1	7.4	0.7	10.8	0.29	721	0.09	0.02492 (0.2)	0.1689	(1.4)	0.0491 (1.3)	158.69	±0.36	158.4	154.4	0.39	2020
sH	1-13	115	3.5	3.9	1.7	1.9	0.36	140	0.12	0.02488 (0.3)	0.1719	(4.4)	0.0501 (4.2)	158.42	±0.43	161.1	200.7	0.69	2020
Western selvege																			
WCB10710 (Bi Hb quartz diorite) 41-549625, -123-440581; single youngest point, 1 xeno																			
el sA	0-61	295	7.6	4.6	1.0	4.4	0.42	290	0.14	0.02500 (0.2)	0.1710	(3.8)	0.0496 (3.7)	159.17	±0.33	160.2	176.2	0.62	2017
eq sB	2-88	72	2.0	5.6	3.3	1.6	0.44	116	0.14	0.02487 (0.4)	0.1666	(10.0)	0.0486 (9.7)	158.34	±0.65	156.5	128.8	0.77	2017
Lower zone																			
WCB2008 (Bi Hb quartz diorite) 41-644450, -123-306239; 159.69 ± 0.23 Ma weighted mean 6/8, 2 points, MSWD 3.1																			
sC	27-00	17	0.5	12.6	3.0	10.5	0.46	256	0.15	0.02512 (0.2)	0.1759	(3.2)	0.0508 (3.0)	159.95	±0.38	164.6	231.2	0.52	2012
sH	3-78	171	4.7	17.8	1.6	12.0	0.59	651	0.19	0.02506 (0.2)	0.1687	(1.7)	0.0488 (1.6)	159.54	±0.28	158.3	139.9	0.50	2017
WCB 176 (Bi Hb quartz diorite) 41-506850, -123-327828; single point, 1 xeno																			
WCB 176 sD	8-43	89	2.3	19.3	1.2	16.4	0.44	1032	0.14	0.02521 (0.6)	0.1692	(1.5)	0.0487 (1.3)	160.48	±0.96	158.7	132.3	0.46	2012
Stinkard pluton																			
WCB8409 (Bi Hb tonalite) 41-69039758, -123-1799854; 158.81 ± 0.23 Ma (2σ), MSWD 2.4), 2 points, 5 antecrystic or single youngest plus 6 ante																			
sA	4-00	297	8.0	32.2	4.5	6.7	0.38	439	0.12	0.02491 (0.2)	0.1688	(1.5)	0.0491 (1.4)	158.61	±0.34	158.4	154.9	0.40	2012
sC	10-54	63	1.7	17.7	2.1	8.0	0.31	534	0.10	0.02529 (0.5)	0.1695	(1.6)	0.0486 (1.4)	161.01	±0.86	158.9	128.2	0.44	2017
sB	47-25	81	2.0	96.1	2.0	47.5	0.32	3069	0.10	0.02502 (0.1)	0.1701	(0.3)	0.0493 (0.2)	159.30	±0.23	159.5	161.9	0.56	2017
sD	6-75	88	2.7	18.0	4.2	3.6	0.35	244	0.11	0.02497 (0.2)	0.1700	(1.4)	0.0494 (1.3)	158.98	±0.32	159.4	166.0	0.41	2020
sE	4-50	216	5.2	23.3	0.6	36.9	0.19	2482	0.06	0.02506 (0.2)	0.1703	(0.5)	0.0493 (0.4)	159.56	±0.31	159.7	162.1	0.47	2020
sF	25-30	129	3.4	84.8	4.7	17.3	0.32	1130	0.10	0.02519 (0.4)	0.1688	(0.7)	0.0489 (0.5)	160.39	±0.68	159.3	142.5	0.68	2020
sG	24-60	102	3.0	74.8	11.9	5.4	0.41	354	0.13	0.02509 (0.2)	0.1719	(0.6)	0.0497 (0.6)	159.75	±0.31	161.1	180.9	0.43	2020
WCB9009 (Bi Px gabbro-diorite) 41-66139771, -123-1140949; 158.80 ± 0.18 Ma, 95% confid., MSWD 0.61, 5 points, 2 antecrystic, X/Y/Z uncertainties ± 0.18/0.19/0.25 Ma																			
sF	4-73	91	2.8	13.1	2.9	3.9	0.43	254	0.17	0.02503 (0.2)	0.1672	(1.8)	0.0484 (1.7)	159.34	±0.29	157.0	121.1	0.43	2017
sG	3-60	123	3.8	13.6	3.1	3.7	0.58	244	0.15	0.02505 (0.3)	0.1707	(1.5)	0.0494 (1.4)	159.48	±0.50	160.0	167.9	0.39	2017
sH	3-38	110	3.4	11.6	2.6	3.9	0.67	246	0.21	0.02493 (0.2)	0.1702	(1.7)	0.0495 (1.6)	158.76	±0.27	159.6	171.6	0.49	2017
sI	2-25	56	1.4	3.3	0.9	3.5	0.45	235	0.14	0.02501 (0.3)	0.1724	(4.0)	0.0500 (3.9)	159.22	±0.47	161.5	194.9	0.60	2020
sJ	1-62	123	4.1	6.7	2.5	2.1	0.52	146	0.17	0.02498 (0.3)	0.1706	(3.6)	0.0495 (3.4)	159.03	±0.45	160.0	173.8	0.61	2020

(continued)

Table 1: Continued

Sample	Weight U (µg)	Pb (ppm)	Sample cPb Pb (pg)	Pb*/Pbc	Th/U	Corrected atomic ratios				206/238 Th date (Ma)	err	207/235 date (Ma)	207/206 Th date (Ma)	Rho	Run date						
						²⁰⁶ Pb/ ²⁰⁴ Pb	²⁰⁸ Pb/ ²⁰⁶ Pb	²⁰⁶ Pb/ ²³⁸ U Th (rad.)	²⁰⁷ Pb/ ²³⁵ U (rad.)							²⁰⁷ Pb/ ²⁰⁶ Pb Th (rad.)	%err	%err	%err		
sK	5.40	119	3.1	16.8	0.5	36.9	0.51	2271	0.16	0.02498	(0.2)	0.1701	(0.5)	0.0494	(0.5)	159.06	±0.28	159.5	166.3	0.43	2020
sL	3.24	195	5.0	16.2	0.9	17.7	0.45	1115	0.14	0.02493	(0.2)	0.1696	(0.9)	0.0493	(0.8)	158.75	±0.30	159.1	164.4	0.38	2020
<i>Misc. single points¹</i>																					
MMB377 sB	0.51	999	27.7	14.0	1.3	10.8	0.68	651	0.22	0.02497	(0.2)	0.1706	(1.4)	0.0495	(1.3)	159.01	±0.28	159.9	173.8	0.46	2017
WCB8009 sA	2.60	583	14.7	38.3	3.0	12.4	0.36	805	0.11	0.02464	(0.3)	0.1654	(1.8)	0.0487	(1.7)	156.92	±0.54	155.4	132.0	0.42	2012
WCB2108 sA	11.25	508	12.3	139	1.8	77.0	0.32	4923	0.10	0.02450	(0.2)	0.1659	(0.3)	0.0491	(0.3)	156.06	±0.25	155.9	153.2	0.55	2012
WCB 6209 sB	11.25	85	2.1	23.9	2.1	11.3	0.38	727	0.12	0.02490	(0.3)	0.1698	(1.5)	0.0495	(1.4)	158.56	±0.41	159.3	169.8	0.35	2012

Sample: eu, euhedral; eq, equant; el, elongate; s, single grain; g, number of grains. Weight represents estimated weight after first step of CA-TIMS zircon dissolution and is only approximate. U and Pb concentrations are based on this weight and are useful for internal comparisons only. Picograms (pg) sample and common Pb from the second dissolution step are measured directly, however, and are accurate. Sample Pb is sample Pb (radiogenic + initial) corrected for laboratory blank. cPb is total common Pb; 2 pg or 1 pg (2012 or 2017–2020 respectively) was assigned to laboratory blank depending on the year processed. Pb*/Pbc is radiogenic Pb to total common Pb (blank + initial) Corrected atomic ratios: ²⁰⁶Pb/²⁰⁴Pb is corrected for mass discrimination and tracer; all others are corrected for blank, mass discrimination, tracer and initial Pb; values in parentheses are 2σ errors in per cent. Rho is ²⁰⁶Pb/²³⁸U vs ²⁰⁷Pb/²³⁵U error correlation coefficient. Superscript Th indicates ²⁰⁶Pb/²³⁸U and ²⁰⁷Pb/²³⁵U ratios and dates corrected for Th-disequilibrium following Schärer (1984) assuming magma Th/U of 2.2. Run date: data were acquired during three periods with slightly different mass discrimination and Pb blank isotopic compositions. Bi, biotite; Hb, hornblende; Px, pyroxene.

¹Rock types and locations are as follows. Late-stage units: MMB377 (hornblende biotite granite, southern Wooley Creek batholith); 41-3854, –123-3885, WCB8009 (biotite hornblende granodiorite, upper zone); 41-47055015, –123-4153859; WCB2108 (two-mica granite, Slinkard pluton); 41-826267, –123-183667. Central zone: WCB 6209 (biotite hornblende quartz diorite); 41-57735527, –123-3548798.

Zircon dissolution and chemistry were adapted from methods developed by Krogh (1973), Parrish et al. (1987) and Mattinson (2005). All zircons were chemically abraded (CA-TIMS). Final dissolutions were spiked with a mixed ²⁰⁶Pb/²³⁵U tracer (ET535). Pb and UO₂ from zircons were loaded onto single rhenium filaments with silica gel without any ion exchange cleanup; isotopic compositions were measured in single Daly-photomultiplier mode on a Micromass Sector 54 TMS system at the University of Wyoming. Data were acquired over an 8 year period with slight variations in mass discrimination, blank amounts, and isotopic composition of the Pb blank. Mass discrimination for Pb was based on replicate analyses of NIST SRM 981, determined as 0.196 ± 0.10, 0.217 ± 0.12, and 0.248 ± 0.16% per a.m.u. for 2012, 2017 and 2020 respectively. U fractionation was determined internally during each run. Measured procedural blanks ranged from 2 to 0.38 pg Pb during the course of the study. U blanks were 0.1 to 0.001 pg. Isotopic composition of the Pb blank as 206/204, 207/204 and 208/204 was measured as 18.6387 ± 0.38, 15.5593 ± 0.52, 37.8471 ± 1.73 for 2012 and 18.572 ± 0.39, 15.731 ± 0.41, 38.38 ± 0.94 from 2017 to 2020. Concordia coordinates, intercepts, uncertainties and concordia ages were calculated using PBMacDAT and ISOPLOT programs (based on Ludwig 1988, 1991, 1998). The decay constants used by PBMacDAT are those recommended by the IUGS Subcommittee on Geochronology (Steiger & Jäger, 1977): 0.155125 × 10⁻⁹ a⁻¹ for ²³⁸U, 0.98485 × 10⁻⁹ a⁻¹ for ²³⁵U and present-day ²³⁸U/²³⁵U = 137.88.

Table 2: Summary, zircon oxygen isotope data

Sample	Rock type	Comment	$\delta^{18}\text{O}$ (‰), V-SMOW	$\pm 2\sigma$	<i>n</i>
<i>Slinkard pluton lower-zone equivalent</i>					
WCB-9009	gabbro-diorite		7.45	0.20	13
<i>Slinkard pluton late granite</i>					
WCB-2108	2-mica granite	all grains	9.57	1.63	15
WCB-2108		high omitted	9.42	0.90	14
<i>Lower zone, WCB</i>					
WCB-1408	tonalite	all grains	7.29	0.92	17
WCB-1408		low omitted	7.38	0.46	16
WCB-2008	quartz diorite		7.61	0.52	16
<i>Central zone, WCB</i>					
WCB-4809	quartz diorite		8.34	0.86	6
WCB-4809		low 2 omitted	8.60	0.38	4
WCB-4909	quartz diorite		7.16	0.52	17
WCB-5809	leucodiorite		6.72	0.56	10
WCB-6209	quartz diorite		8.06	0.30	8
WCB-6209		low 7	7.96	0.58	7
Z5	tonalite		7.32	0.38	12
<i>Upper zone, WCB</i>					
WCB-2309	granodiorite		7.65	0.68	18
WCB-7809	granodiorite		7.67	0.50	15
WCB-7909	tonalite		7.65	0.46	16
<i>Southern mafic selvage</i>					
WCB-2408	diorite		7.47	0.32	10
<i>Late granite, WCB</i>					
MMB-377	granite	all grains	8.81	2.1	9
		low 4	7.79	0.74	4
		high 5	9.63	0.92	5

determined using the SHRIMP-RG were collected over three rounds of analysis. The ages measured during the first two rounds agree with CA-ID-TIMS ages; however, ages measured during the third round are consistently younger than CA-ID-TIMS and LA-ICP-MS ages by as much as a few million years (Supplementary Data File 1). Therefore, in Fig. 6b both SHRIMP-RG and LA-ICP-MS spot ages that are within error of or older than CA-ID-TIMS ages are plotted but ages younger than CA-ID-TIMS results are excluded.

On the basis of the new high-precision CA-ID-TIMS ages, we modify the interpretation of Coint *et al.* (2013b) in outlining the sequence of assembly of the plutonic system. We interpret emplacement of the main stage lower zone from *c.* 160 to 158.80 ± 0.18 Ma, whereas the upper-zone ages are 158.50 ± 0.20 Ma to 157.68 ± 0.18 Ma, making the upper and lower zones seemingly temporally distinct from one another. The new single crystal 156.92 ± 0.54 Ma age of sample WCB-8009 indicates that parts of the upper zone remained in the magmatic state as much as 0.5 Myr longer than the rest of the zone.

Two samples from the central zone yielded ages identical to those from the lower zone, whereas three samples yielded ages identical to those for the upper zone (Supplementary Data File 1). These ages are consistent with the interpretation of the central zone as the transition between upper and lower units. It is noteworthy that sample Z5 (159.01 ± 0.20 Ma) was collected because field relations indicated it to be the youngest tonalitic sheet in the outcrop area—the same area from which sample WCB4909 (158.30 ± 0.16 Ma) was collected. These data, along with presence of abundant,

variably disrupted synplutonic dikes and enclave swarms (Barnes *et al.*, 1986a; Coint *et al.*, 2013b) indicate that in addition to marking the transition between upper and lower zones, the central zone was a focus of episodic magma emplacement, mixing, and mingling over most of the lifetime of the system.

Two samples from the western selvage (WCB-10510 and -10710) yielded distinct ages of 159.28 ± 0.17 and 158.34 ± 0.65 Ma, respectively, mirroring the difference in ages between lower and upper zones. These results indicate that rocks of the selvage initially crystallized from lower-zone magmas and were then either intruded by or locally mingled with upper-zone magmas. In contrast, the dated southern selvage sample (WCB-2408) gave an age identical to upper-zone samples: 158.32 ± 0.32 Ma.

With an age of 156.06 ± 0.25 Ma, the SP two-mica granite is significantly younger than the rest of the SP. This age difference is consistent with near-pervasive development of magmatic and sub-solidus fabrics in the older rocks of the SP, but the lack of such fabrics in the two-mica granite (Allen, 1981). The late-stage Bt granite body that intrudes the upper zone (Fig. 1) yielded an age of 155.0 ± 1.7 Ma from four concordant analyses by SHRIMP-RG (Supplementary Data File 1). This age contrasts with a single-crystal CA-ID-TIMS age of 159.01 ± 0.28 Ma. The latter age is inconsistent with geological relationships and is considered to represent an antecryst, as discussed in the following section.

In summary, the CA-ID-TIMS data indicate that the WCB-SP system represents *c.* 4 Myr (159.95 ± 0.38 to 156.06 ± 0.25 Ma) of magmatic activity. Because the oldest age from the western selvage is identical to that of

Table 3: Sm–Nd isotope data for xenoliths, plutonic rocks, and host terranes

Sample no.	Location	Sm (ppm)	Nd (ppm)	$^{147}\text{Sm}/^{144}\text{Nd}^1$	$^{143}\text{Nd}/^{144}\text{Nd}^2$	ϵ_{Nd}^3 (at 158 Ma)	T_{DM}^4 (Ma)
<i>Xenoliths</i>							
MMB-7a	Bear Creek	2.32	9	0.1555	0.512724 ± 9	2.5	853
MMB-180	Hooligan Lake	2.36	10.06	0.1417	0.512834 ± 7	4.9	477
MMB-219a	Pleasant Lake	2.94	17.9	0.09934	0.511825 ± 9	−14	1619
MMB-332b	Ten Bear Mt	8.44	46.13	0.1106	0.511536 ± 9	−19.8	2225
MMB-340	Ukonom Lake	3.97	14.52	0.1651	0.512705 ± 9	1.9	1069
MMB-344	west of Burney Lake	1.3	5.31	0.1483	0.512819 ± 11	4.5	555
MMB-80085	Pleasant Lake	3.15	14.14	0.1347	0.512775 ± 8	3.9	544
WCB-5309	Pigeon Roost trail	2.87	9.75	0.1778	0.512998 ± 8	7.4	285
WCB-7009	Granite Lakes basin	5.58	26.53	0.1271	0.511487 ± 9	−21.1	2752
WCB-7009@2	[duplicate]	5.53	26.52	0.1261	0.511471 ± 9	−21.4	2750
WCB-111	Ten Bear Mt	9.79	63.76	0.09278	0.511662 ± 8	−17	1735
WCB-112	Ten Bear Mt	6.93	37.76	0.1109	0.511542 ± 7	−19.7	2222
WCB-124a	Pleasant Lake	3.12	14.2	0.1326	0.512169 ± 8	−7.9	1637
WCB-142	Salmon River	6.56	30.39	0.1305	0.512049 ± 8	−10.2	1814
WCB-144	Salmon River	6.46	42.63	0.09161	0.511434 ± 11	−21.4	2003
<i>Host rocks</i> ⁵							
MMB-614B	wHt, Wooley Creek trail	4.8	19.82	0.1465	0.512941 ± 8	6.9	282
KM40A	wHt, Orleans, CA area	3.57	15.1	0.1427	0.512928 ± 7	6.7	294
WCB-140	eHt, Salmon River road	8.25	47.75	0.1045	0.511329 ± 9	−23.7	2391
KM10-9	eHt, Salmon River road	3.97	17.04	0.141	0.512232 ± 9	−6.9	1694
WCB-8209	RCt, Tomkins Crrek area	2.19	8.85	0.1499	0.512865 ± 9	5.3	464
WCB-8609a	RCt, Tomkins Creek area	2.67	8.47	0.1907	0.513023 ± 8	7.6	281
<i>Plutonic rocks</i>							
WCB-132	Pigeon Roost trail	2.26	8.46	0.1612	0.512780 ± 12	3.4	787
MMB-645A	gabbro, Slinkard pluton	1.86	6.64	0.1695	0.512826 ± 5	4.2	777
MMB-342	tonalite, lower zone	3.18	14.14	0.1362	0.512798 ± 6	4.3	512
WCB-1408	tonalite, lower zone	2.38	10.39	0.1383	0.512771 ± 6	3.7	576
WCB-4809	quartz diorite, central zone	4.73	20.49	0.1395	0.512774 ± 6	3.8	580
WCB-4909	quartz diorite, central zone	4.99	21.29	0.1418	0.512769 ± 6	3.6	607
MMB-317	quartz monzodiorite, upper zone	3.49	15.74	0.1341	0.512775 ± 6	3.9	540
MMB-379	tonalite, near base of upper zone	3.82	18.14	0.1275	0.512748 ± 6	3.5	546
MMB-394	granodiorite, evolved upper zone	1.55	7.94	0.1184	0.512725 ± 9	3.2	532
MMB-471	granodiorite, upper zone	2.83	14.2	0.1206	0.512750 ± 6	3.7	505
MMB-594	quartz diorite, western selvage	3.45	15.59	0.1339	0.512815 ± 6	4.7	467
MMB-18879	diorite, synplutonic dike	3.53	14.79	0.1443	0.512784 ± 6	3.9	597
MMB-201	gabbro, synplutonic dike	4.13	16.86	0.148	0.512926 ± 6	6.5	321
MMB-377A	late-stage titanite-bearing granite	3.59	18.87	0.115	0.512789 ± 6	4.5	420

Whole-rock Sm–Nd isotope data by ID-TIMS were obtained at the Geological Survey of Finland (GTK) by O. T. Rämö (October 2011, April 2012, February 2013).

¹Error on $^{147}\text{Sm}/^{144}\text{Nd}$ is 0.5%.

² $^{143}\text{Nd}/^{144}\text{Nd}$ normalized to $^{146}\text{Nd}/^{144}\text{Nd} = 0.7219$; reported error is $2\sigma_m$ in last significant digit.

³Initial ϵ_{Nd} value, calculated at 158 Ma using chondritic values of $^{143}\text{Nd}/^{144}\text{Nd} = 0.51264$ and $^{147}\text{Sm}/^{144}\text{Nd} = 0.1966$.

⁴Depleted mantle model age (DePaolo, 1981).

5wHt, western Hayfork terrane; eHt, eastern Hayfork terrane; RCt, Rattlesnake Creek terrane.

the lower zone, the selvage is interpreted to mark the original western (upper) extent of lower-zone magmas. The bulk of the upper zone was assembled in <4 Myr, but magmatic activity continued for at least an additional million years. Evidently, upper-zone magmas locally mixed or mingled with lower-zone magmas, as indicated by the range of ages in the central zone and the western selvage.

Older zircons in the plutons

All three dating methods identified individual crystals whose ages are older than intrusive ages determined by CA-ID-TIMS. Concordant ages of these older zircons are primarily 170–161 Ma, with a scattering of ages between 195 and 170 Ma (Fig. 6b). The majority of these older ages were determined on oscillatory-zoned crystals, which suggests that they were magmatic in origin (e.g. Corfu *et al.*, 2003). Among the 498 zircons dated by

SHRIMP-RG and LA-ICP-MS, some 38 grains yielded ages statistically older than the lower zone.

Xenoliths

U–Pb ages of zircon from six xenoliths were determined by SHRIMP-RG. All reported ages are ^{204}Pb -corrected $^{206}\text{Pb}/^{238}\text{U}$ ages; the data are illustrated in Fig. 7. Three xenoliths are from the lower zone (MMB-79, MMB-799b, and WCB-5309), one is from the lower- to central-zone transition (MMB-219a), one is from the central zone (WCB-7009), and one is from the western selvage (MMB-332b; Fig. 2). Only two zircons were recovered from MMB-79 and both gave discordant dates, 162.5 ± 5.0 and 163.9 ± 2.4 Ma. Thirteen zircons from sample MMB-799B yielded 10 concordant ages from 167.5 to 155.9 Ma (Fig. 7a). If the oldest four, high-U ages are excluded, the weighted average date for seven zircons <58% discordant is 158.0 ± 0.7 Ma [mean

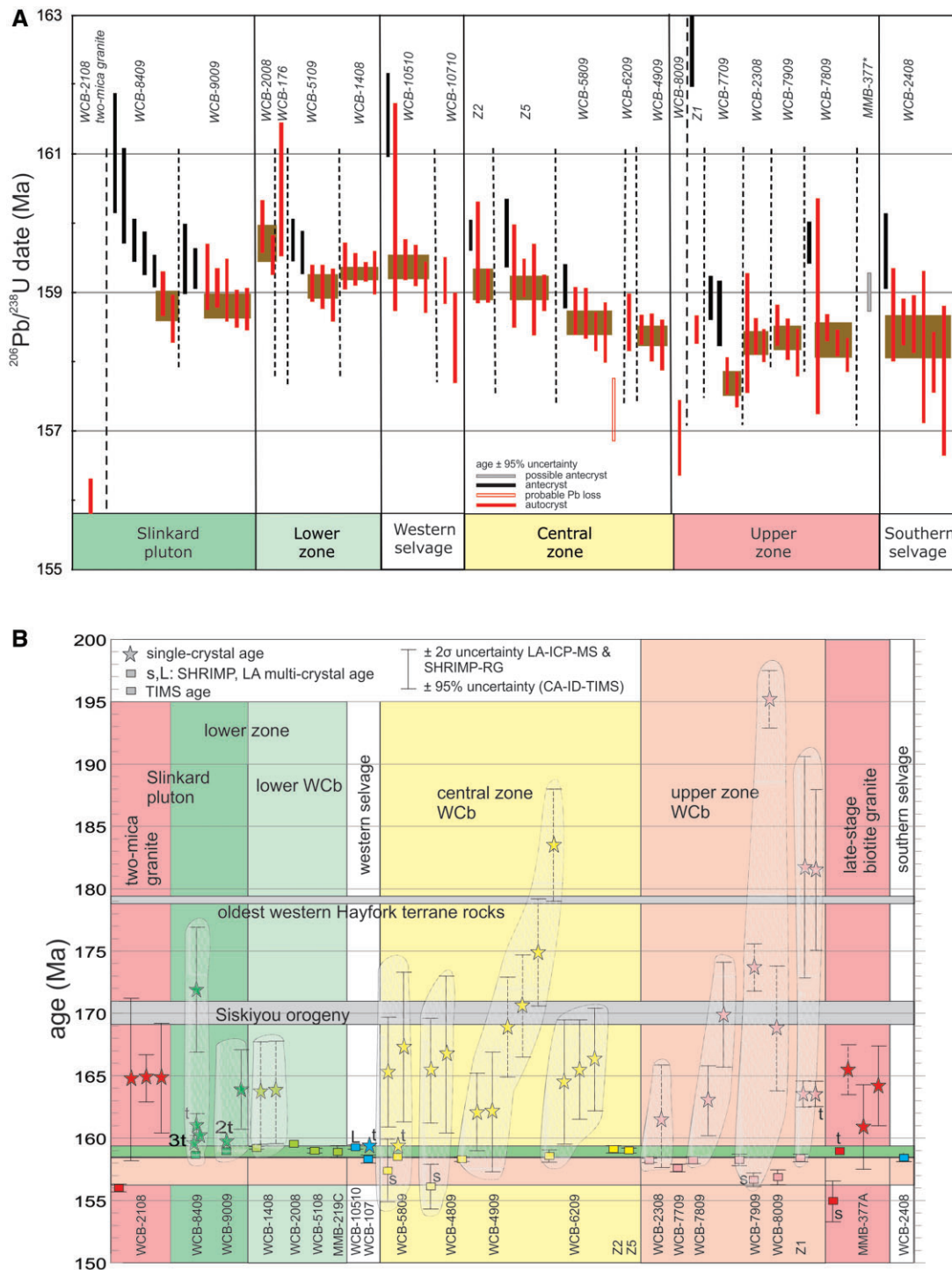


Fig. 6. (a) Plot of complete CA-ID-TIMS data (Coint *et al.*, 2013b; this work). Broad brown fields indicate analyses used to calculate the U–Pb ages in Table 1. (b) Summary of U–Pb (zircon) ages for the WCB and Slinkard pluton. Unlabelled squares represent weighted average ages determined by CA-ID-TIMS (a). Uncertainties on CA-ID-TIMS are 95%. Labelled squares (s and L) are weighted averages of dates from SHRIMP-RG and LA-MC-ICP-MS, respectively, with 2σ uncertainties. Stars represent single-crystal ages of xenocrysts and antecrysts by SHRIMP (continuous lines), LA-MC-ICP-MS (dashed lines), and CA-ID-TIMS. The CA-ID-TIMS ages are labelled with a t for single analyses, 2t for two analyses, and 3t for three analyses (see the text for discussion). Horizontal gray bars indicate the approximate ranges of regional geological events. The horizontal green bar represents the range of emplacement ages of the lower zone. The horizontal pink bar represents the range of emplacement ages of the upper zone. Red symbols represent late-stage granites. Shaded balloons enclose data from a single sample.

square weighted deviation (MSWD) = 1.2]. Similarly, sample WCB-5309 yielded eight concordant to weakly discordant dates from 157.0 ± 2.2 to 160.3 ± 3.0 Ma

(Fig. 7b) and a weighted mean age of 158.4 ± 1.0 Ma (MSWD = 0.73). Three additional zircons yielded ages from 163.1 ± 3.2 to 164.3 ± 1.6 Ma.

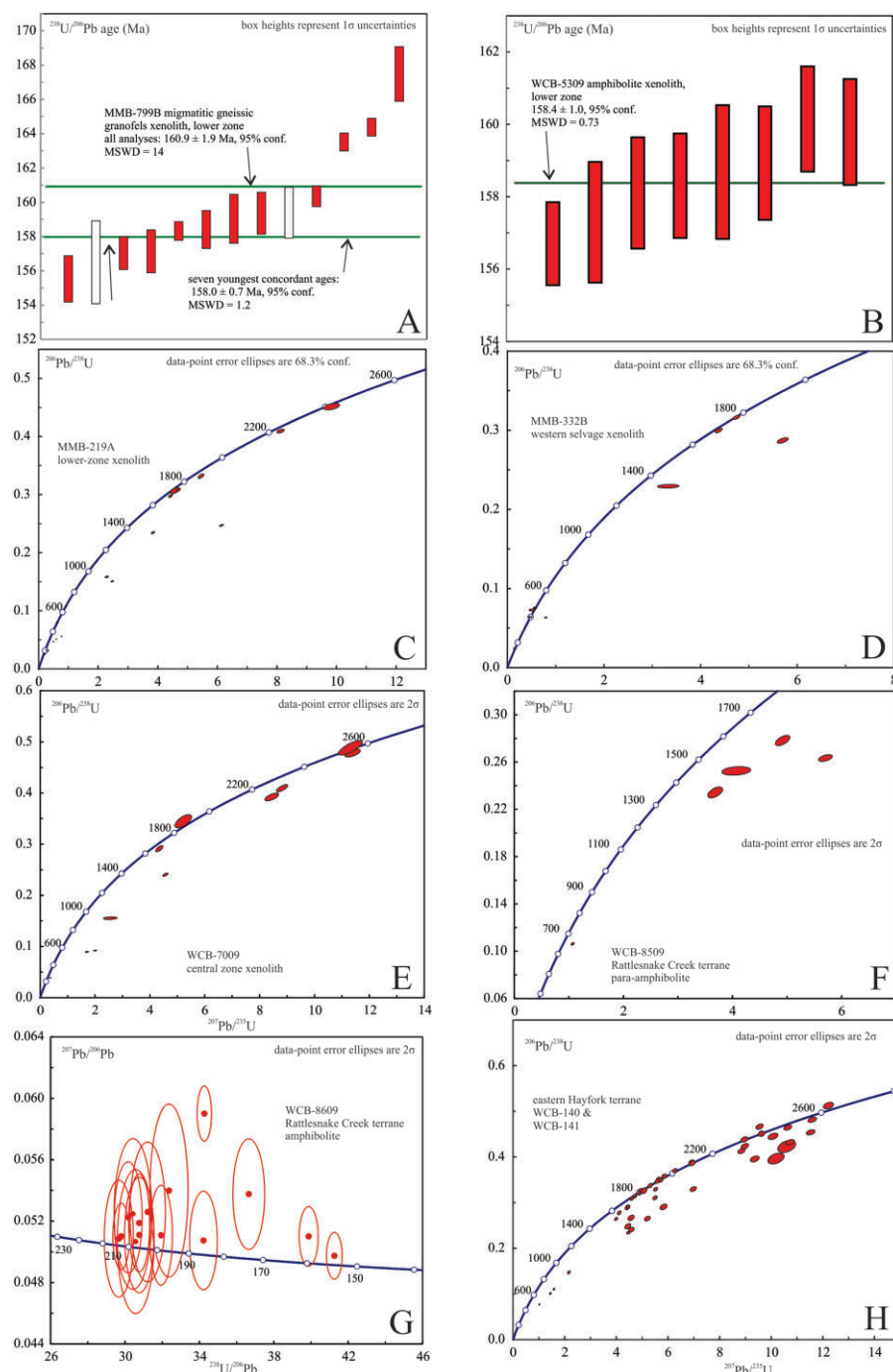


Fig. 7. U–Pb (zircon) data on xenoliths and host rocks. (a) Migmatitic xenolith from the lower zone. Two weighted average ages are shown, one for all concordant grains and one for the seven youngest concordant grains. Unfilled symbols indicate discordant dates. (b) Weighted average age of an amphibolite xenolith from the lower zone. (c–e) Concordia diagrams illustrating detrital zircon ages from xenoliths with eastern Hayfork terrane affinities. (f) Concordia diagram of zircon-poor para-amphibolite from the Rattlesnake Creek terrane. (g) Tera–Wasserburg diagram of zircons from a para-amphibolite from the Rattlesnake Creek terrane. (h) Concordia diagram of pooled detrital zircon samples from the eastern Hayfork terrane.

The transitional lower- to central-zone xenolith (MMB-219a) yielded a wide range of variably concordant ages: from 2403 ± 32 Ma (concordant) to 161.3 ± 5.4 Ma (discordant) (Fig. 7c). The xenolith from the western selvage (MMB-332B) contains zircons with ages from 1773 ± 17 to 155.9 ± 3.2 Ma (Fig. 7d). Sample

WCB-7009 is a quartzite xenolith from the central zone. Zircons from this sample yielded six concordant ages from 2559 ± 51 to 1641 ± 24.4 Ma and five discordant ages from 1382 ± 14 to 234.6 ± 2.0 Ma (Fig. 7e). It is noteworthy that samples MMB-219a and MMB-332B contained zircons with concordant ages ranging from

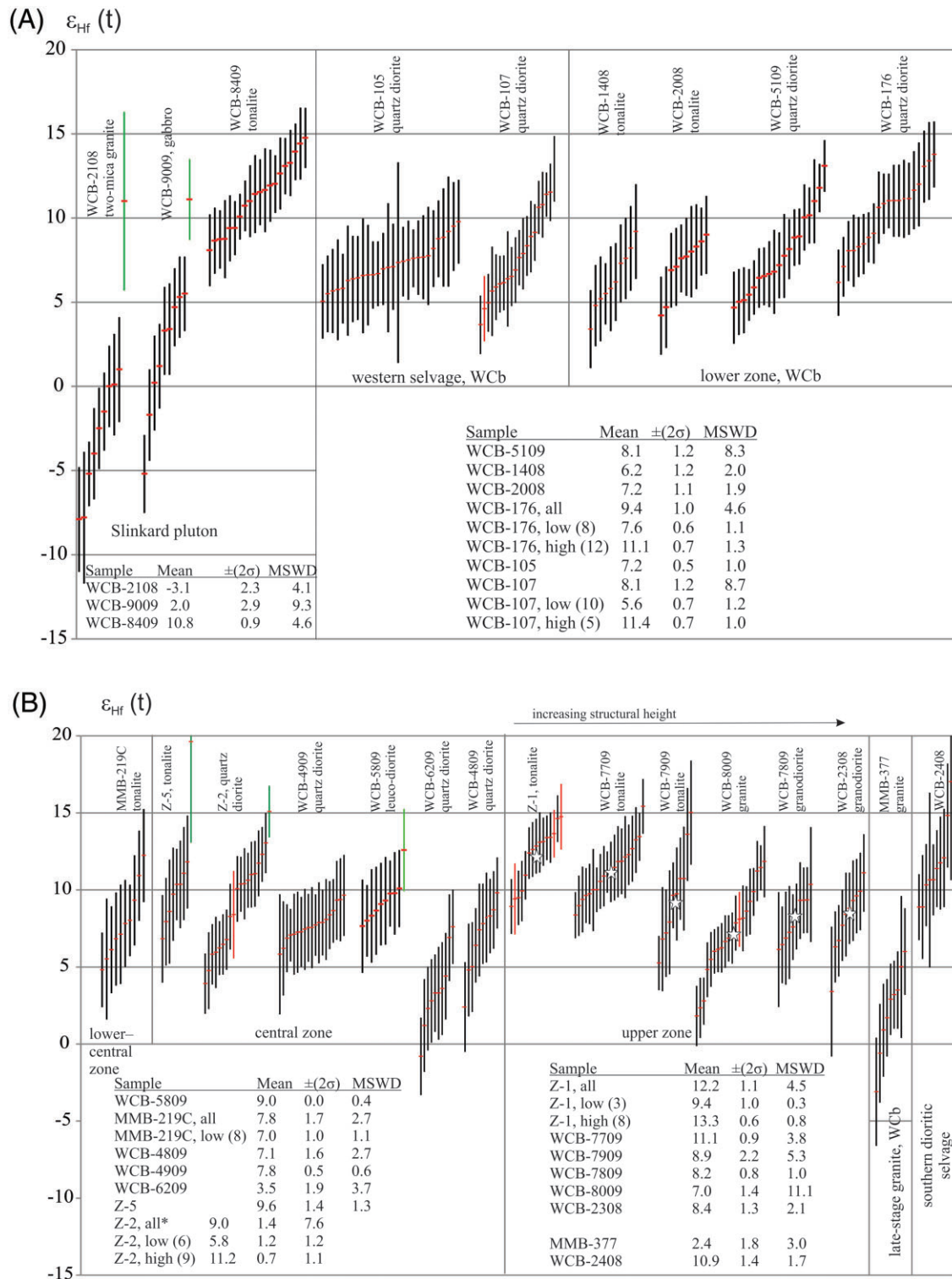


Fig. 8. Zircon ϵ_{Hf} values. Inset tables give weighted averages for each sample. For samples with highly variable ϵ_{Hf} values, two additional averages show differences in split populations. In (a) and (b), ϵ_{Hf} was calculated for the age of the individual spot analysis. In (c), ϵ_{Hf} was calculated at 158 Ma. Plotted uncertainties are 2σ . In (a) and (b), green bars indicate data not included in the weighted average, and red bars indicate zircons with discordant ages. (a) Lower zone (Slinkard pluton and lower zone of the WCB) and western mafic selvage. (b) Lower- to central-zone transition, central and upper zones, southern late-stage biotite granite, and southern mafic selvage. For upper-zone samples, stars indicate average ϵ_{Hf} , illustrating the decrease in ϵ_{Hf} structurally upward. (c) Xenoliths in the WCB.

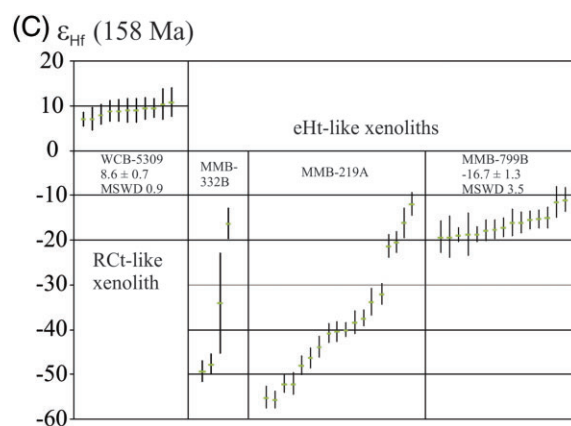


Fig. 8. Continued.

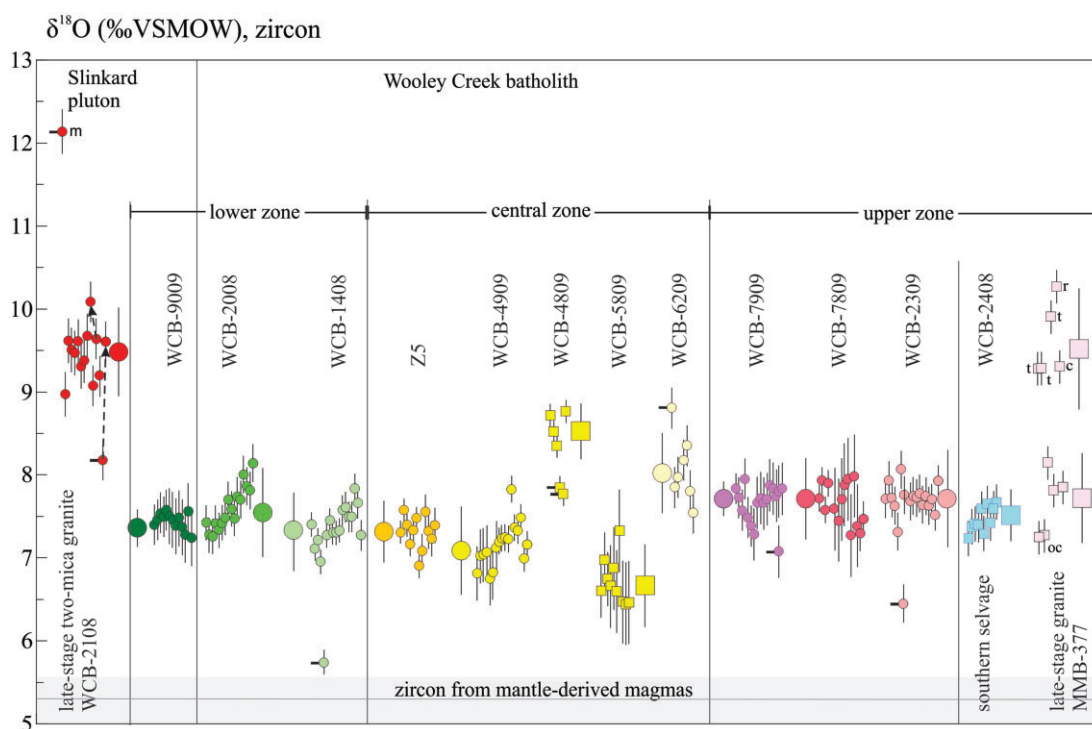


Fig. 9. Zircon oxygen isotope values measured by SIMS. Small symbols are individual spot analyses with error bars indicating two standard deviation precision. Large symbols are mean values with error bars that represent two standard deviations (Table 2). Spot analyses with an adjacent tick mark (–) were not included in the mean. For two-mica granite sample WCB-2108, dashed arrows connect core to rim compositions and label ‘m’ indicates a crystal mantle composition. For late-stage Hbl-bearing Bt granite sample MMB-377, two mean values were calculated, one for high $\delta^{18}\text{O}$ values and one for lower values. Labels adjacent to MMB-377 spot analyses are t (prism tip), c (core), and oc (outer core). Horizontal bar represents zircon from mantle-derived magmas from [Lackey et al. \(2005\)](#).

400 to 494 Ma. This time interval is characteristic of some of the oldest magmatism in the Klamath Mountain province (see Discussion).

Host rocks

Zircons from three RCT para-amphibolites that are host to the SP (WCB-8209, 8509, and 8609) were dated by SHRIMP-RG. Only two zircons were recovered from WCB-8209; they yielded ^{204}Pb -corrected $^{206}\text{Pb}/^{238}\text{U}$ ages of 777.3 ± 5.8 Ma (discordant) and 2231 ± 3.4 Ma

(concordant). Five discordant zircon ages from WCB-8509 vary from 1580 to 647 Ma (Fig. 7f). In contrast, 14 zircons from WCB-8609 yielded ages from 212 to 154 Ma (Fig. 7g). Many of these ages are concordant, although ages younger than c. 195 Ma are too young to represent depositional ages of the RCT (e.g. [Wright & Wyld, 1994](#)). The weighted average of the oldest five grains is 211.2 ± 1.8 Ma (MSWD = 1.52).

Two samples of the eHt (WCB-140 and 141) were collected along the southwestern WCB contact (Fig. 1) and detrital zircons were dated by LA-ICP-MS. The pooled

results of 48 analyses yielded ages from 2669 to 479 Ma, with a majority of Meso- and Paleoproterozoic ages (Fig. 7h). Two grains gave ages of 72.6 and 70.9 Ma and one gave an age of 158.7 Ma. Although the latter age could represent zircon growth during contact metamorphism, it is more likely that all three zircons are the result of laboratory contamination; they are excluded from later discussion.

Hf isotopes, zircon

The ε_{Hf} values for WCB–SP zircons are plotted in Fig. 8, along with tabulated weighted mean values. Some samples in each zone yielded zircons with statistically identical ε_{Hf} values, whereas other samples contained zircons whose ε_{Hf} values cannot be explained as a single population (e.g. compare sample WCB-10510, with $\text{MSWD} = 1.0$, with sample WCB-5109, with $\text{MSWD} = 8.3$; Fig. 8a). Four samples contain zircons with negative ε_{Hf} values: the two late-stage granites, Slinkard pluton gabbro-diorite sample WCB-9009, and central-zone sample WCB-6209 (Fig. 8a and b); these samples also have the lowest average ε_{Hf} values (Fig. 8).

Hf isotopes were also measured on zircon from four xenoliths (Fig. 8c). In sample WCB-5309, ε_{Hf} values are tightly clustered and all zircons yielded U–Pb ages identical to the magmatic age (158.4 ± 1.0 Ma). Zircons in the remaining three xenolith samples yield mainly negative ε_{Hf} values. In samples MMB-332B (western selvage) and MMB-219A (central- to lower-zone transition), ε_{Hf} (158 Ma) ranges widely, as is consistent with the range of concordant U–Pb ages in these samples, as old as c. 1790 Ma in MMB-332B and c. 2400 Ma in MMB-219A (Fig. 7). In contrast, although sample MMB-799A has zircons that yield low ε_{Hf} values, the age of these zircons is the age of magmatism (c. 158.0 ± 0.7 Ma).

Oxygen isotopes

Bulk-rock $\delta^{18}\text{O}$ data for plutonic rocks, xenoliths, and two host-rock samples were presented by Barnes *et al.* (1990). All but two samples of the main stage varied from 7.8 to 9.9‰, with two Slinkard pluton samples at 10.7 and 12.2‰. These latter two samples probably reflect late-stage hydrothermal alteration. Late-stage granite samples ranged in $\delta^{18}\text{O}$ from 11.2 to 12.2‰. One sample of eastern Hayfork terrane host rock yielded 15.0‰ and one sample from the western Hayfork terrane gave a value of 10.2‰. The $\delta^{18}\text{O}$ values of three xenoliths, all of which will be shown below to have eastern Hayfork terrane protoliths, yielded values from 9.0 to 10.9‰.

Individual $\delta^{18}\text{O}$ values of zircon ($\delta^{18}\text{O}_{\text{Zr}}$) along with average values are plotted in Fig. 9 and summarized in Table 2. Three mafic lower-zone samples yield identical average $\delta^{18}\text{O}_{\text{Zr}}$ values of c. 7.49‰ (Fig. 9) and, similarly, three upper-zone samples yield identical average values of c. 7.67‰. The $\delta^{18}\text{O}_{\text{Zr}}$ values in gabbro sample WCB-9009 from the SP form a tight group with $\delta^{18}\text{O}_{\text{Zr}}$ 7.45 ± 0.09 ‰ (Table 2). In contrast, average $\delta^{18}\text{O}_{\text{Zr}}$ values from the central zone range from 6.7 to 8.3‰

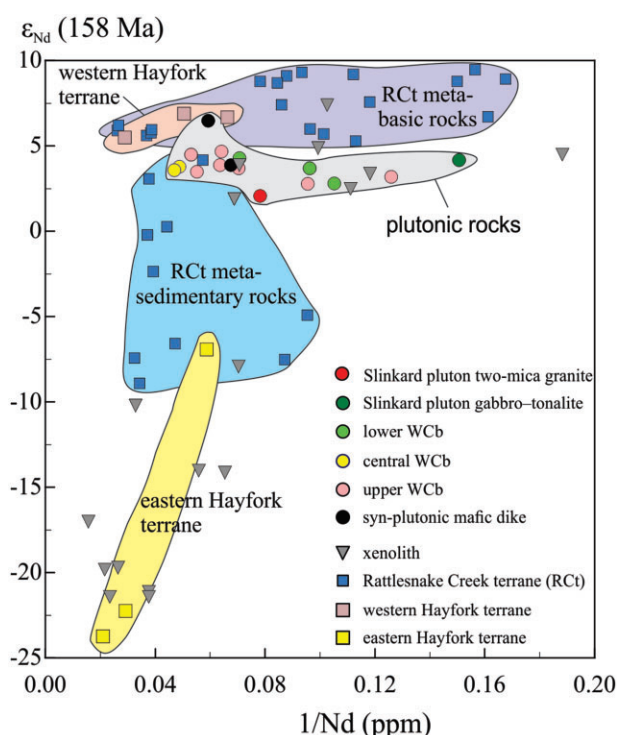


Fig. 10. Bulk-rock ε_{Nd} at 158 Ma plotted versus $1/\text{Nd}$. Thirty-six new data for xenoliths, host rocks, and the WCB–SP combined with published data from Barnes *et al.* (1992), Wright & Wyld (1994), and Frost *et al.* (2006). The colored fields outline the range of values of the WCB–SP and host terranes. Rocks of the Rattlesnake Creek terrane are divided into high- ε_{Nd} metabasic rocks (Wright & Wyld, 1994; this work) and variable ε_{Nd} meta-sedimentary rocks (see Frost *et al.*, 2006). Xenolith ε_{Nd} values encompass the entire range of host-rock values, whereas the plutonic rocks occupy a small range of ε_{Nd} values.

(Fig. 9; Table 2) and extend both below and above average values for lower and upper zones. Moreover, no correlation between sample age and $\delta^{18}\text{O}_{\text{Zr}}$ is evident.

The average $\delta^{18}\text{O}_{\text{Zr}}$ value of zircon from the late-stage SP two-mica granite (sample WCB-2108; 9.5 ± 0.2 ‰; Table 2) is higher than that for all main-stage samples and is consistent with the higher bulk-rock $\delta^{18}\text{O}$ values (see above). Individual analyses display greater dispersion than main-stage data (Fig. 9) and two grains display zoning, with rim values higher than core values (Fig. 9). One analysis (grain 12-1; Fig. 9) yielded a $\delta^{18}\text{O}_{\text{Zr}}$ value of 12.1‰. This analysis is from a CL-dark core zone that lacks visible inclusions or cracks.

The $\delta^{18}\text{O}_{\text{Zr}}$ values of the late-stage Hbl-bearing Bt granite in the southern WCB (MMB-377) are bimodal, in contrast to all other samples. Four grains yielded an average of 7.8 ± 0.6 ‰, which is identical to $\delta^{18}\text{O}_{\text{Zr}}$ values of upper-zone zircons. These analyses are from crystal interiors. Five grains yielded an average of 9.6 ± 0.6 ‰. All but one of these analyses are of crystal rims (Fig. 9).

Nd isotopes

The new whole-rock Nd isotope data (Table 3) are compared with published data in Fig. 10. All data are bulk

analyses and ϵ_{Nd} values are calculated to 158 Ma. All WCB–SP samples occupy a narrow range of ϵ_{Nd} +2.1 to +4.5, except for one synplutonic dike with ϵ_{Nd} of +6.5. There is no obvious correlation between ϵ_{Nd} and $1/\text{Nd}$ (Fig. 10).

In contrast, ϵ_{Nd} values of the three host rock terranes display considerable variation. Three samples of the wHt, a volcanic cobble, a crystal-lithic arenite, and an argillite, are nearly identical (+5.5 to +6.9; Table 3; Barnes *et al.*, 1992). These data are within the range of ϵ_{Nd} values of metabasic rocks from the RCt (Wright & Wyld, 1994; Fig. 10). In contrast, clastic metasedimentary rocks from the cover sequence of the RCt display ϵ_{Nd} from +4.2 to –8.9 (Frost *et al.*, 2006; Fig. 10). Samples of the eHt are distinct in displaying negative ϵ_{Nd} (–6.9 to –23.7; Table 3; Barnes *et al.*, 1992), and slightly overlap the field of RCt cover sequence metasedimentary rocks (Fig. 10). Xenoliths from the WCB span virtually the entire range of ϵ_{Nd} values observed in the host rocks (Fig. 10; Table 3) but tend to display values less than –8 or greater than +1.9.

DISCUSSION

Timing and sequence of magma emplacement

High-precision dating by CA-ID-TIMS indicates that emplacement of WCB–SP magmas ranged from 160 to 156 Ma, with the main volume of the system emplaced from 159.8 to 157.2 Ma. The final stages of pluton assembly occurred at c. 156 Ma with emplacement of minor parts of the upper zone (sample WCB-8009) and the two late-stage granites. Magmas were emplaced into three stacked tectonostratigraphic terranes: the Rattlesnake Creek terrane, overlain by the western Hayfork terrane, in turn overlain by the eastern Hayfork terrane. Although we divide the plutonic system into an older lower zone, a transitional central, and a younger upper zone, two features are particularly noteworthy. First, the lower zone was emplaced across all three host terranes, whereas the upper zone intrudes only the upper two terranes (Fig. 1). Second, parts of the western mafic selvage are identical in age, mineral assemblage, and composition to the lower zone (Barnes, 1983, 1986a, 1990; Coint *et al.*, 2013a), although it is now separated from the lower zone by upper- and central-zone rocks (Fig. 1). Therefore, we infer that a large proportion of the existing plutonic system was initially occupied by lower-zone-type magmas, and that these rocks or magmas were displaced by, or recycled into upper-zone magmas. Similar recycling was reported for the much larger Tuolumne Intrusive Complex (Paterson *et al.*, 2016).

Provenance of xenoliths—a ghost stratigraphy

One of the goals of this research was to identify the origins of xenoliths. In some cases, the source is clear-cut. For example, amphibolite, metagabbro, and metaserpentinite are common only in the RCt mélangé; quartz-

rich rocks (metachert and quartzite) are most abundant in the eHt; and in the wHt, coarse clinopyroxene grains are characteristic of both metasandstone and metavolcanic rocks (Wright & Fahan, 1988; Donato *et al.*, 1996; Barnes & Barnes, 2020). However, all three terranes contain metabasite and argillite, and marble is common in the RCt and eHt. Moreover, many metabasite and argillitic xenoliths are migmatitic (Fig. 3), having undergone partial melting during and after incorporation into the pluton, and are difficult to correlate with host rocks on the basis of mesoscopic features.

Xenoliths of peridotite, metagabbro, and amphibolite are restricted to the parts of the lower zone that intrude the RCt (Fig. 2). They are thus interpreted as being derived from the ophiolitic mélangé section of the RCt. Many xenoliths in the lower zone are schistose to gneissic migmatite and some display granofels texture. These xenoliths have positive ϵ_{Nd} (+1.9 to +7.4; Table 3; Fig. 10), although only one displays ϵ_{Nd} typical of RCt metabasite (WCB-5309, ϵ_{Nd} +7.4). The slightly lower ϵ_{Nd} values could reflect alternative sources (RCt metasedimentary rocks and/or the wHt) or could result from isotopic exchange between the xenolith and host magma. The potential for such exchange is evident in the fact that these xenoliths underwent partial melting after being surrounded by the host magmas. In some samples, partial melting was accompanied by crystallization of zircon, as illustrated by the 158.4 ± 1.0 Ma age of zircons from xenolith WCB-5309 (Fig. 7). Zircons in this sample yielded ϵ_{Hf} (158 Ma) of $+8.6 \pm 0.7$, which is lower than expected in a rock with bulk ϵ_{Nd} of +7.4. Thus, as with Nd isotopes, it is possible that the zircon ϵ_{Hf} values reflect hybridization of leucosome melts with melts from the surrounding magma. Migmatitic xenolith MMB-180 (Fig. 2) also yielded a positive ϵ_{Nd} value (+4.9). However, this xenolith and others in the same area feature relict pyroxene phenocrysts, which indicate derivation from the western Hayfork terrane.

Xenoliths collected from the central zone, from near the western contact of the lower zone, and from the southern selvage are typically gneissic to granoblastic migmatite, but also include calc-silicates, metapelites and quartzite (Fig. 2). These migmatitic and quartzite xenoliths have ϵ_{Nd} from –7.9 to –21.4 (Table 3). In most samples, zircons are detrital, with ages as old as Neoproterozoic, common Paleoproterozoic-age grains, and scant but characteristic Ordovician and Silurian dates (Fig. 7). These age and isotopic features indicate that most, if not all, of these xenoliths are from the eHt (Figs 2, 7, and 10; Table 3; see Ernst *et al.*, 2017, for additional eHt zircon data). Several of these xenoliths yielded Jurassic zircon ages, although the depositional age of the eastern Hayfork terrane is Triassic (Ernst *et al.*, 2017). Thus, we interpret the Jurassic-age zircon as formed during partial melting. An extreme example is xenolith MMB-799B, in which all zircons yielded Jurassic dates, with a weighted mean age of 160.9 ± 1.9 Ma (Fig. 7a). The average ϵ_{Hf} value of these zircons is -16.7 ± 1.3 (MSWD 3.5), indicating that the

composition of the melt phase in this xenolith reflects the bulk composition of the xenolith. In contrast, detrital zircons from two other xenoliths with eHt-like features display ϵ_{Hf} (158 Ma) values that span a range from -12 to -56 (Fig. 8c).

In summary, the combination of lithological features, zircon ages and Hf isotope ratios, and bulk-rock Nd isotope data allows us to interpret the provenance of xenoliths in the WCB (Fig. 2). Xenoliths from the RCt are restricted to the deepest structural levels and xenoliths from the wHt are located along the western selvage and in the southern parts of the lower zone. Xenoliths from the eHt are common in the central zone and the transition between lower and central zones, and are locally present near contacts with the eHt (Fig. 2). Thus, the distribution of xenoliths in the WCB preserves a ghost stratigraphy that accords with the stacking of host terranes, from lowest RCt to highest eHt.

It is noteworthy that xenoliths are most abundant in the lower and central zones and are uncommon in the upper zone. This difference in relative abundance may be related to the fact that the lower and central zones were emplaced incrementally as intrusive sheets (Coint *et al.*, 2013a), a process that would permit entrapment of host rocks. In contrast, even if the upper zone were emplaced incrementally, the nearly identical compositions and zoning patterns of hornblende from the upper zone indicate that upper-zone magmas underwent convective overturn (Coint *et al.*, 2013b; Barnes *et al.*, 2016a), which would have erased evidence for incremental emplacement.

Antecrysts and xenocrysts

In what follows, the term autocryst refers to zircons whose U–Pb ages are, within analytical uncertainty, the same as CA-ID-TIMS ages, antecrysts are grains whose ages indicate that they may be related to precursor magmatism, and xenocrysts are grains too old to be related to magmatic activity (e.g. Bacon & Lowenstern, 2005; Miller *et al.*, 2007). Xenocrysts could be inherited from a deep crustal source region or be related to assimilation of host rocks.

Each unit of the WCB–SP contains zircons in the age range 170–160 Ma, some of which overlap with emplacement ages (Fig. 6). In addition, each unit contains a few zircon grains older than c. 170 Ma. The 170–160 Ma interval spans the time from the end of the tectonism associated with the Siskiyou orogeny at c. 170 Ma (Barnes *et al.*, 2006) to c. 160 Ma initial emplacement of the WCB–SP. Siskiyou tectonic activity involved significant crustal thickening owing to terrane imbrication along regional thrust faults (Coleman *et al.*, 1988; Barnes & Allen, 2006) and marked the end of Middle Jurassic wHt arc magmatism (Barnes & Barnes, 2020). Plutons emplaced after Siskiyou orogenesis, such as the WCB–SP, display isotopic evidence for a significant crustal component, particularly from oxygen isotope data (Barnes *et al.*, 1990; Allen & Barnes, 2006), whereas

older magmatic suites lack such evidence. These results were interpreted to indicate that, as a consequence of terrane imbrication during Siskiyou tectonism, metasedimentary rocks were accreted to the lower Klamath crust. Thus, the few zircons with ages older than c. 170 Ma are thought to be inherited crystals from these lower-crustal metasedimentary rocks. Although these zircons could be xenocrysts from the wHt, zircons are exceedingly rare in the wHt (two zircon grains found in >150 thin sections of the unit). Likewise, the 195–181 Ma age range is too young for the zircons to be xenocrysts from the RCt or eHt.

It is also noteworthy that despite the presence of Proterozoic and Paleozoic zircons in many xenoliths and two host terranes (Fig. 7), no such zircons were analyzed in any main- or late-stage sample. To understand the relative paucity of zircon antecrysts and xenocrysts (of any age) we investigated magmatic temperatures to determine the likelihood of zircon stability during pluton assembly.

Liquidus temperatures of lower- and central-zone magmas were in the range 1168–1084 °C (Barnes *et al.*, 2016a) for magmas parental to quartz diorite and tonalite and were higher for magmas parental to (zircon-poor) diorite to gab fbro. Trace element zoning patterns in augite from these rocks (Coint *et al.*, 2013a) revealed that Zr was an incompatible element during augite crystallization. This relationship is illustrated in Supplemental Data Fig. 1, in which increasing Zr is shown to be anticorrelated with the Eu anomaly in augite (panel A) and positively correlated with increasing total REE abundances (panel B). We further tested conditions of zircon stability by analysis of trace element zoning patterns in hornblende (Supplemental Data Fig. 1C; Barnes *et al.*, 2016b, 2019). In this diagram, Ti is a proxy for temperature, with T decreasing with decreasing Ti (Otten, 1984; Pe-Piper, 1988; Ernst & Liu, 1998) and the Zr/Hf ratio as a marker for zircon fractionation (Bea *et al.*, 2006; Claiborne *et al.*, 2006). Zircon fractionation results in decreasing Zr/Hf, whereas fractionation of hornblende and plagioclase have a negligible effect on the ratio (Bea *et al.*, 2006). At Ti contents >14 000 ppm, hornblende from all three zones displays constant Zr/Hf values; however, at Ti contents less than c. 14 000 ppm, the Zr/Hf ratio begins to decrease in nearly all central- and upper-zone hornblende, as well as in some lower-zone hornblende. This change in slope occurs at a temperature of c. 800 °C [compare the Putirka (2016) hornblende thermometer], thus indicating that zircon became stable at T much lower than emplacement T (Barnes *et al.*, 2019).

We conclude that virtually all zircon autocrysts from main-stage units of the WCB–SP crystallized at ≤ 800 °C. This conclusion explains the small proportion of xenocrysts and of potential antecrysts, most of which would have dissolved in the host magma. It is also consistent with textural data: in lower-zone rocks zircon is intergranular among quartz and plagioclase and never included in pyroxene. In central- and upper-zone rocks zircon is

interstitial and occurs as inclusions in hornblende and biotite. The most significant consequence of this conclusion is that it requires that the Hf and oxygen isotopic diversity displayed by autocrystic zircon in main-stage rocks reflects mainly *in situ* processes, not inheritance.

These conclusions do not relate to the two late-stage granites, both of which contain 170–160 Ma zircon grains (Fig. 6). There is scant major element variation within these two bodies (Barnes *et al.*, 1990) and neither contains mafic enclaves. However, the southern Hbl-bearing Bt granite locally engulfed rocks of the upper zone, which may explain the bimodal distribution of $\delta^{18}\text{O}$, with lower $\delta^{18}\text{O}$ zircons from the host upper-zone rocks and higher $\delta^{18}\text{O}$ zircons reflective of a lower-crustal source.

Isotopic heterogeneity in the main stage

Variation of Hf isotope ratios in main-stage magmatic zircon is too large to be explained by closed-system differentiation (Fig. 8), because crystal fractionation should not change ε_{Hf} values. Similarly, although bulk-rock $\delta^{18}\text{O}$ values may change by 1.0–1.5‰ owing to crystal fractionation (e.g. Bucholz *et al.*, 2017), closed-system changes in $\delta^{18}\text{O}_{\text{Zr}}$ vary by a few tenths of a per mil (Lackey *et al.* 2008). Thus, the $\delta^{18}\text{O}_{\text{Zr}}$ values in all WCB–SP samples are significantly higher than can be explained by crystal fractionation from a mantle-derived basaltic parent (c. 5.5‰; Lackey *et al.*, 2005). Moreover, the range of oxygen isotope ratios in the central-zone samples, all of which are tonalite (Fig. 9), is inconsistent with closed-system processes. These observations lead to the questions: is the isotopic variability related to deep-seated MASH process such as crustal melting and mixing of crust-derived with mantle-derived magmas (Allen & Barnes, 2006), or is the variability explained by open-system processes (assimilation and mafic recharge) at the level of emplacement (Barnes *et al.*, 1986a, 1987, 1990), or were both processes important? Any explanation must accommodate several critical observations: (1) high magmatic temperatures preclude significant zircon inheritance from lower-crustal sources and/or MASH zones; (2) variation of ε_{Hf} and $\delta^{18}\text{O}_{\text{Zr}}$ in many samples cannot represent zircon crystallization from a homogeneous melt (Figs 8 and 9); (3) no sample displays $\delta^{18}\text{O}_{\text{Zr}}$ characteristic of crystallization from a mantle-derived melt (Fig. 9); (4) the most evolved Hf and O isotope values (lowest ε_{Hf} and highest $\delta^{18}\text{O}$) characterize late-stage two-mica and Hbl-bearing Bt granite (Figs 8 and 9).

We postulate that these observations are best explained by magma evolution in a vertically extensive magma column. Initially, mantle-derived basaltic magmas ponded in a lower-crustal MASH zone, where they mixed with crust-derived felsic magmas. The isotopic compositions of these basaltic magmas are hinted at by isotopic data from a few of the mafic enclaves and synplutonic dikes in the WCB and the nearby Grayback pluton, in which the lowest initial $^{87}\text{Sr}/^{86}\text{Sr}$ values range from 0.7027 to 0.7036 and the highest ε_{Nd} values range from 8.1 to 10.2 (Barnes *et al.*, 1990, 1992, 1995). These data indicate that basaltic magma entering the lower

crust displayed depleted mantle-like isotopic compositions. However, the lowest $\delta^{18}\text{O}$ (zircon) values measured in the WCB–SP are c. +6.5‰, and most are greater than +7‰. Likewise, average ε_{Hf} (zircon) values are lower than expected from Jurassic depleted mantle (e.g. Vervoort & Blichert-Toft, 1999). We interpret the higher $\delta^{18}\text{O}_{\text{Zr}}$ and lower ε_{Hf} values as baseline values that resulted from lower-crustal MASH-zone interaction of mantle-derived basaltic magmas with melts derived from metasedimentary rocks (see Allen & Barnes, 2006).

Magmas rising from the MASH zone were mainly intermediate in composition (Barnes *et al.*, 2016a) and still at temperatures higher than zircon stability, as indicated by pyroxene thermometry (see above). Therefore, the magmas carried few or no entrained zircons to the emplacement level, which means that the intra-sample isotopic variability in zircon crystals must represent heterogeneity within individual melt increments (batches) from which zircon crystallized. This heterogeneity may be explained as follows: (1) the melt phase within individual magma batches retained significant Hf and oxygen isotopic heterogeneity during transport from the lower to the middle crust, and this heterogeneity was recorded during *in situ* crystallization of magmatic zircon; or (2) individual magma batches underwent a combination of mixing with mafic recharge magmas and assimilation of melts derived from host-rock xenoliths at the level of emplacement.

The first possibility is difficult to support because transport of magmas from a lower-crustal MASH zone to the mid-crustal emplacement site, a distance of c. 15 km (Barnes *et al.*, 1986b; Barnes & Allen, 2006) probably homogenized any isotopic heterogeneity inherited from the MASH zone. If so, then the isotopic heterogeneities must represent *in situ* mixing and assimilation.

The effects of *in situ* open-system behavior would depend on the level of emplacement in the system (ghost stratigraphy reflected in xenolith compositions), the isotopic leverage provided by xenoliths from each host-rock unit, the melt productivity of these xenoliths, the relative proportions of xenolith-derived melts, and, potentially, the amount of added mafic recharge magmas. An example of the last possibility comes from comparison of samples WCB-4809 and WCB-4909, which were collected adjacent to one another. The former sample lacks mafic enclaves and contains zircon with average $\delta^{18}\text{O}_{\text{Zr}}$ of 8.5‰; the latter sample contains mafic enclaves and contains zircon with average $\delta^{18}\text{O}_{\text{Zr}}$ of 7.0‰ (Fig. 9). In the following section, these variables are discussed for the three main zones of the system, and then for the last-stage granites.

Open-system processes during pluton assembly

Lower zone

Construction of the lower zone began via multiple injections of predominantly intermediate magmas (Coint *et al.*, 2013b; Barnes *et al.*, 2016a) with episodic intrusion of mafic magmas to form synplutonic dikes. We include the western selvage as part of lower-zone

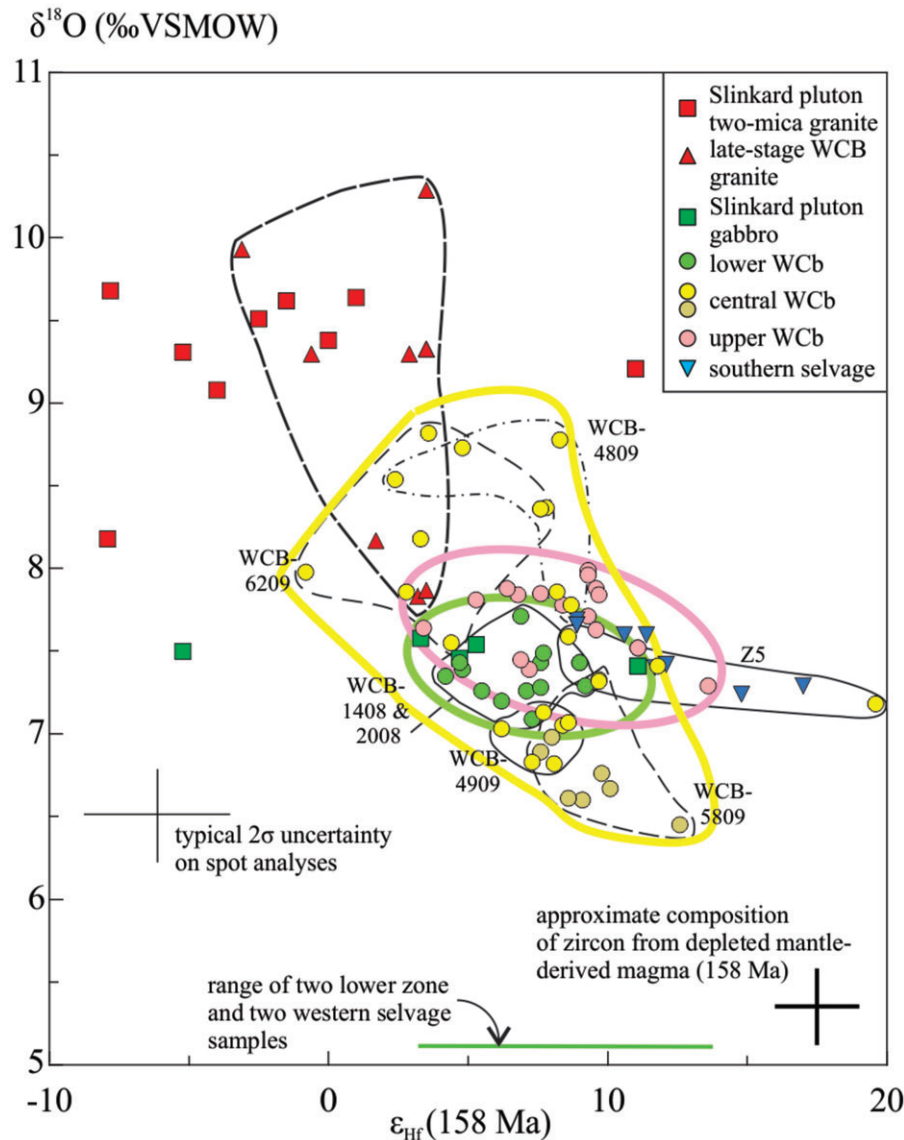


Fig. 11. Zircon oxygen isotope values plotted against ϵ_{Hf} (158 Ma). The colored outlines enclose samples from the lower zone (green), central zone (yellow), and upper zone (pink). Continuous and dashed lines enclose ranges of individual samples, as labeled.

magmatism because of its overlapping U–Pb age and similarities in bulk-composition, mineral assemblages, and zircon isotope values. Inclusion of the western selvage in the lower zone means that the original volume of lower zone was significantly larger than would be inferred from the present outcrop area and that lower-zone magmas intruded all three host terranes (Fig. 1). Emplacement of lower-zone magmas as sheets engulfed host rocks as large screens, which were repeatedly injected by later magma batches (e.g. Fig. 3a and d) and disrupted to form xenoliths and xenolith swarms. Many screens and xenoliths partially melted, as indicated by field and textural observations (Figs 3a, b and 4) and zircon U–Pb ages identical to the ages of zircons in the plutonic rocks (Fig. 7a and b).

Xenoliths from all three host terranes are present in the lower zone (Fig. 2). If bulk-rock ϵ_{Nd} values (Fig. 10; Table 3) are a guide to zircon ϵ_{Hf} values, as is typical,

then assimilation of melts from xenoliths from the RCT and wHt would have little effect on magmatic ϵ_{Hf} values. However, all three units contain metasedimentary rocks, assimilation of which could raise $\delta^{18}\text{O}$ in the magma. Such assimilation is hinted at in the spread of $\delta^{18}\text{O}$ values in samples WCB-1408 and -2008 (Fig. 9). These samples were collected from a part of the lower zone that intrudes both RCT and eHt (Fig. 2). Nevertheless, lower-zone zircons display the smallest amount of Hf and oxygen isotope variability in the system (Fig. 11).

Central and upper zones

As lower-zone magmatism waned, magma emplacement shifted upward, into and above the structurally highest parts of the lower zone, to form a sill- or tongue-like body that extended south from what is now the central zone (Fig. 1; Barnes, 1983). These upper-

zone magmas were of intermediate composition, most were emplaced in less than 0.5 Myr (c. 158.6–158.2 Ma), and they were accompanied by intrusion of mafic dikes. We suggest that central-zone geology preserves the state of the system during the transition from lower- to upper-zone activity. This state includes relatively abundant xenoliths, the majority of which are from the eHt (Fig. 2). Because of the low and variable ε_{Nd} and ε_{Hf} (Table 3 and Fig. 8, respectively) and the high $\delta^{18}\text{O}$ of eHt xenoliths (9.0–10.9‰), *in situ* assimilation and magma mixing resulted in the range of isotopic values seen in zircon from the central zone.

In this model, we would expect most of what is now the upper zone to be similar to the central zone: characterized by intense mingling and mixing of intermediate and mafic magmas, a lack of temporal or spatial compositional zoning, and the greatest diversity in zircon Hf and oxygen isotopes. Instead, the upper zone grades upward in terms of increasing SiO_2 and decreasing MgO and FeO (Barnes *et al.*, 1986a, 2016a) and decreasing average ε_{Hf} (zircon; Fig. 8b), but uniform $\delta^{18}\text{O}_{\text{Zr}}$.

Previous work (Barnes, 1983; Coint *et al.*, 2013a; Barnes *et al.*, 2016a) documented changes in mafic magmatic enclave abundances and geological features in the upper zone. In structurally lower parts of the zone, dense enclave swarms and pillowed enclaves are common. With increasing structural height, enclave swarms are less abundant and enclaves in the swarms are more dispersed, until in the structurally highest regions only isolated enclaves are present. The above-cited researchers also showed that hornblende compositions are nearly identical throughout the upper zone.

These features can be explained as the result of (1) relatively rapid emplacement of crystal-poor upper-zone magmas, (2) influx and ponding of mafic magmas near the base of the upper zone, (3) convective circulation caused by emplacement of these mafic magmas (see Burgisser & Bergantz, 2011), and (4) consequent homogenization of magma compositions. During and after convective mixing, melt-rich magmas migrated upward, leading to the upward transition from tonalite to granite (Fig. 1; Barnes *et al.*, 2016a).

A question remains: what process explains the diversity of zircon ε_{Hf} values in many samples (Fig. 8) compared with the relatively small intra-sample ranges of zircon $\delta^{18}\text{O}$? We suggest that mixing of host magmas with xenolith-derived melts was commonly chaotic (e.g. Perugini & Poli, 2004; Perugini *et al.*, 2006, 2008). Such mixing involves intricate folding of the distinct magmas, resulting in alternating filaments of host- and xenolith-derived melts (fig. 1 of Perugini & Poli, 2004). Diffusive exchange of oxygen between compositionally distinct filaments would be relatively fast in hydrous magmas (Zhang & Ni, 2010), whereas diffusion of quadrivalent ions such as Zr and Hf would be much slower (e.g. Perugini *et al.*, 2008). We suggest that zircon crystallized during and after such mixing, so that rapid diffusion of oxygen resulted in relatively uniform $\delta^{18}\text{O}_{\text{Zrn}}$ values in both types of melt, whereas slow

diffusion of Hf resulted in a range of Hf isotope values that are reflected in the wide range of intrasample zircon ε_{Hf} .

This mixing process explains oxygen isotope features in both central- and upper-zone zircon. In the central zone, local mixing of numerous, isotopically variable xenolith melts would yield individual magma batches with a range of $\delta^{18}\text{O}_{\text{Zrn}}$ values that were still internally homogeneous. In contrast, convection in the upper zone was at a much larger scale (e.g. Coint *et al.*, 2013a; Barnes *et al.*, 2016b) and led to overall uniform $\delta^{18}\text{O}_{\text{Zrn}}$ values, yet still diverse ε_{Hf} values, as zircon crystallized.

Isotope models

The emplacement scenario above calls on *in situ* contamination of MASH-zone-derived magmas by assimilation of melts from host-rock xenoliths. This process was modeled for Hf and oxygen isotope compositions using energy-constrained assimilation–fractional crystallization equations (Spera & Bohrsen, 2001; Bohrsen & Spera, 2007). Details of these models are provided in Supplemental Data File 2. The models indicate that isotopic compositions are reached at $T > 830^\circ\text{C}$ and as high as 960°C . The ratio of mass of material assimilated relative to the mass of crystals formed (Ma/Mc) typically varies from c. 0.07 to 0.25.

Although these models explain average zircon isotope data, they do not completely explain some intra-sample Hf isotope variability (Fig. 8). Two examples are central-zone tonalite (Z5) and the sample from the southern selvage, both of which display high ε_{Hf} values and also the relatively high $\delta^{18}\text{O}_{\text{Zr}}$ characteristic to the entire system (Fig. 11). It is likely that the array of zircon compositions in these two samples reflects mixing of magmas with primitive ε_{Hf} and elevated $\delta^{18}\text{O}$ with magmas compositionally similar to the lower zone.

Late-stage granites

By 156 Ma, main-stage magmatism had ended, except for the portion of the upper zone where sample WCB-8009 was collected (Figs 1 and 8b). The similarity of this sample to the rest of the upper zone makes the age peculiar; we ascribe this age to localized rejuvenation of the upper zone, possibly owing to deeper intrusion of mafic magmas.

The two-mica granite in the Slinkard pluton and the Hbl-bearing Bt granite in the southern WCB yielded c. 156 Ma ages, contain zircons with ages from c. 166 to 162 Ma, and have comparatively low ε_{Hf} and high $\delta^{18}\text{O}_{\text{Zrn}}$. The two-mica granite appears to display a unimodal set of $\delta^{18}\text{O}_{\text{Zrn}}$ values (Fig. 9), which we interpret to reflect magma origin from the deep-crustal metasedimentary rocks in which the MASH zone developed. In contrast, the southern Hbl-bearing Bt granite intruded and engulfed rocks of the host upper zone. We therefore suggest that the high- $\delta^{18}\text{O}$ zircon rims in this granite crystallized from a crustal melt, but zircons with lower $\delta^{18}\text{O}$ are xenocrysts from the adjacent main stage of the WCB.

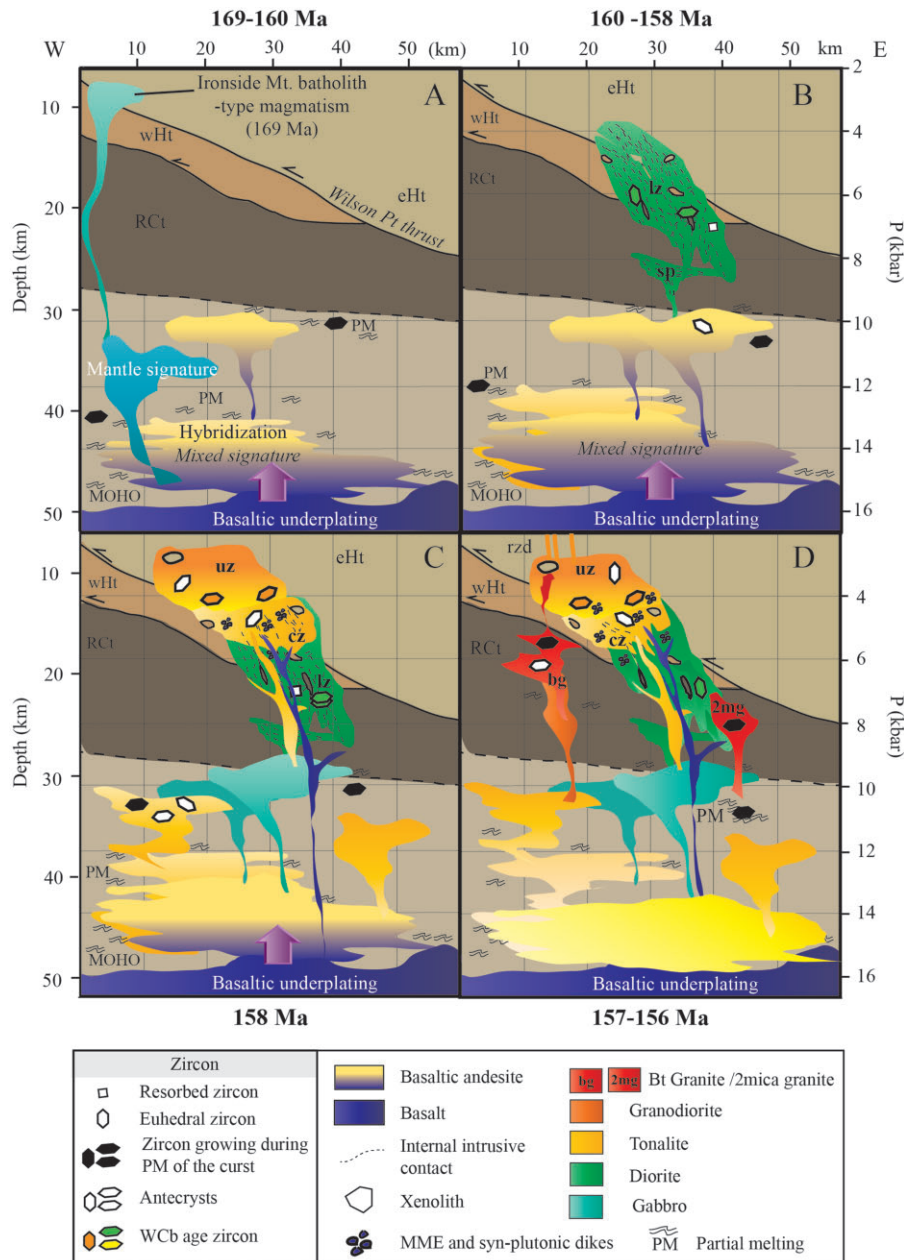


Fig. 12. Schematic growth model for the WCB-SP crustal-scale magmatic system. (a) Initiation of post-Siskiyou magmatism with basaltic magmas underplating and intruding lower crust thickened during the c. 170 Ma Siskiyou orogeny. Orogenic activity emplaced metasedimentary rocks into the lower crust, below the RCt. Oldest post-Siskiyou plutons (e.g. Ironside Mountain batholith) evolved primarily by fractional crystallization, with increasing crustal influence through time. (b) Development of a mature lower-crustal MASH zone and episodic upward emplacement of basaltic through dacitic magmas to form the lower zone (lz: SP and lower WCB). Sheet-like magma batches engulfed host rocks (xenoliths and screens), which partially melted; partial melts then mixed with surrounding magmas. Isotopic leverage during assimilation was primarily associated with eastern Hayfork xenoliths. Emplacement temperatures were higher than zircon saturation temperatures, so the few antecrystic zircons were probably armored. (c) Central zone (cz) and upper zone (uz) of the WCB formed by emplacement of andesitic magmas from the MASH zone into and through the lower zone. The highest levels of lower-zone mushes were intruded by, and locally displaced by upper-zone magmas. Renewed influx of basaltic magma resulted in intense mingling in the central zone (cz) and ponding at the base of the upper zone to form pillowed enclaves and enclave swarms. Heat from this basaltic influx resulted in convection and homogenization of upper-zone (uz) magmas. Post-convection differentiation resulted in upward zonation from tonalite to granite and intrusion of uz magmas as roof-zone dikes (rzd). (d) Late-stage magmatism, with emplacement of the Slinkard two-mica granite (a crustal melt) and southern Hbl-bearing Bt granite (primarily a crustal melt contaminated by assimilation of adjacent upper-zone rocks).

CONCLUSIONS

The WCB-SP are two mid-crustal plutons in which magmatism lasted at least 4 Myr (c. 160–156 Ma), and if

some of the slightly older zircons are antecrysts, then magmatism spanned an even longer time, from c. 164 to 156 Ma (Fig. 12a). Bulk-rock and zircon isotope

systematics are consistent with a model in which primary, mantle-derived magmas ponded and developed a MASH zone in the lower crust, which had been recently thickened during Middle Jurassic orogenesis. Hybridization of basaltic magma with partial melts from metasedimentary lower-crustal rocks imposed elevated $\delta^{18}\text{O}$ and lowered ε_{Hf} and ε_{Nd} compared with depleted mantle. Hybrid magmas from the MASH zone rose into the middle crust, where they formed the WCB–SP (Fig. 12b). These magmas were emplaced at T higher than zircon saturation.

The WCB–SP grew upward, beginning with a lower zone of sheet-like bodies emplaced across all three host terranes, but mainly in ophiolitic mélangé of the RCT (Fig. 12b). Assimilation of RCT xenoliths had minimal isotopic leverage on lower-zone magmas. As lower-zone activity waned, upper-zone magmas were emplaced through and above the lower zone, engulfing wHt and eHt xenoliths (Fig. 12c). Assimilation of these xenoliths resulted in local isotopic heterogeneity, as preserved in the central zone. However, ponding of mafic magma near the base of the upper zone caused convective mixing and homogenization, with consequent homogenization of isotopic compositions. Following convective mixing, upward migration of melt-rich magma led to upward zoning from tonalite to granite.

Magmatism ended with emplacement of late-stage granites: two-mica granite in structurally low levels and Hbl-bearing Bt granite in structurally high levels (Fig. 12d). In both, zircon isotopes indicate primary derivation by lower-crustal melting and, in the case of the Hbl-bearing Bt granite, probably mixing with adjacent main-stage rocks or mush.

Many studies of magmatic systems have ascribed the bulk of differentiation (crustal melting, magma mixing, assimilation, etc.) to the deepest part of the crustal section, with limited modification during transport through the middle crust (e.g. [Annen et al., 2006, 2008](#); [Solano et al., 2012](#)). Other workers have emphasized the potential for crustal assimilation at various levels ([McBirney et al., 1987](#); [Grunder, 1992](#); [Bohrson & Spera, 2001, 2007](#); [Lackey et al., 2005, 2008](#); many others), leading to the concept of crustal magma columns with potential for differentiation at multiple levels (e.g.; [Hildreth, 2004](#); [Walker et al., 2015](#); [Ardill et al., 2018](#); many others). We conclude that the WCB–SP represents a crustal-scale magma system, with a MASH zone at $c.$ 40–50 km, and mid-crustal emplacement from $c.$ 25 to 10 km. Moreover, dikes above the WCB strongly indicate the presence of (now eroded) higher level plutons and/or volcanic strata ([Barnes et al., 1986b](#); [Coint et al., 2013b](#)). Partial melting and assimilation of crustal rocks was not restricted to the MASH zone, but was in fact prominent at the level of emplacement—over a period of more than 2 Myr. Whether clear-cut evidence for emplacement-level assimilation survives cooling and crystallization processes is dependent on the compositions of host rocks, the ability of host-rock xenoliths to

be entrained in the magmas, and magmatic conditions that allow for preservation of isotopic diversity, such as seen in the central zone. Without this preservation, distinguishing between MASH zone versus emplacement-level magmatic processes would be difficult.

We suggest that in relatively hot arc systems, and particularly ones repeatedly refreshed with fluxes of both basaltic and MASH-zone-derived intermediate magmas, mixing and assimilation should be expected through much of the crustal column. Identification of the sites of mixing and the nature of assimilated material clearly requires detailed isotopic analysis of zircon and is greatly enhanced with application of petrological information derived from major and trace element compositions and zoning patterns of the rock-forming minerals.

ACKNOWLEDGEMENTS

We thank Charlotte Allen, Kevin Werts and Aaron Yoshinobu for many discussions about the geology, structure, and evolution of the WCB–SP system, and Joe Wooden for his assistance with, and insight into, SHRIMP-RG data. We thank Olivier Jagoutz and two anonymous reviewers for their journal reviews.

FUNDING

This research was supported by National Science Foundation grants EAR-0838342 to C. Barnes and A. Yoshinobu, EAR-0838546 to K. Chamberlain, and EAR-1524336 to J. Valley. The WiscSIMS lab was supported by NSF EAR-1658823 and the University of Wisconsin-Madison.

SUPPLEMENTARY DATA

Supplementary data are available at *Journal of Petrology* online

REFERENCES

- Allen, C. M. (1981). Intrusive relations and petrography of the Slinkard pluton, central Klamath Mountains, California. Unpublished MS thesis, University of Oregon, Eugene, 120 pp.
- Allen, C. M. & Barnes, C. G. (2006). Ages and some cryptic sources of Mesozoic plutonic rocks in the Klamath Mountains, California and Oregon. In: Snoke, A. W. & Barnes, C. G. (eds) *Geological Studies in the Klamath Mountains Province, California and Oregon: A Volume in Honor of William P. Irwin*. Geological Society of America, *Special Papers* **410**, 223–245.
- Anderson, H. S., Yoshinobu, A. S., Nordgulen, Ø. & Chamberlain, K. (2013). Batholith tectonics: formation and deformation of ghost stratigraphy during assembly of the mid-crustal Andalshatten batholith, central Norway. *Geosphere* **9**, 667–690.
- Annen, C., Blundy, J. D. & Sparks, R. S. J. (2006). The genesis of intermediate and silicic magmas in deep crustal hot zones. *Journal of Petrology* **47**, 505–539.

- Annen, C., Blundy, J. D. & Sparks, R. S. J. (2008). The sources of granitic melt in deep hot zones. *Transactions of the Royal Society of Edinburgh: Earth Sciences* **97**, 297–309.
- Ardill, K., Paterson, S. & Memeti, V. (2018). Spatiotemporal magmatic focusing in upper-mid crustal plutons of the Sierra Nevada arc. *Earth and Planetary Science Letters* **498**, 88–100.
- Bacon, C. R. & Lowenstern, J. B. (2005). Late Pleistocene granodiorite source for recycled zircon and phenocrysts in rhyodacite lava at Crater Lake. *Earth and Planetary Science Letters* **233**, 277–293.
- Barnes, C. G. (1983). Petrology and upward zonation of the Wooley Creek batholith, Klamath Mountains. *Journal of Petrology* **24**, 495–537.
- Barnes, C. G. (1987). Mineralogy of the Wooley Creek batholith, Slinkard pluton, and related dikes, Klamath Mountains, northern California. *American Mineralogist* **72**, 879–901.
- Barnes, C. G. & Allen, C. M. (2006). Depth of origin of late Middle Jurassic garnet andesite, southern Klamath Mountains, California. In: Snoke, A. W. & Barnes, C. G. (eds.) *Geological studies in the Klamath Mountains province, California and Oregon: A volume in honor of William P. Irwin*. Boulder: Geological Society of America, 269–286.
- Barnes, C. G. & Barnes, M. A. (2020). The western Hayfork terrane: Remnants of the Middle Jurassic arc in the Klamath Mountain province. *Geosphere* **16**, 1058–1081.
- Barnes, C. G., Allen, C. M. & Saleeby, J. B. (1986a). Open- and closed-system characteristics of a tilted plutonic system, Klamath Mountains. *Journal of Geophysical Research* **91**, 6073–6090.
- Barnes, C. G., Rice, J. M. & Gribble, R. F. (1986b). Tilted plutons in the Klamath Mountains of California and Oregon. *Journal of Geophysical Research* **91**, 6059–6071.
- Barnes, C. G., Allen, C. M. & Brigham, R. H. (1987). Isotopic heterogeneity in a tilted plutonic system, Klamath Mountains, California. *Geology* **15**, 523–527.
- Barnes, C. G., Allen, C. M., Hoover, J. D. & Brigham, R. H. (1990). Magmatic components of a tilted plutonic system, Klamath Mountains, California. In: Anderson, J. L. (ed.) *The Nature and Origin of Cordilleran Magmatism*. *Geological Society of America, Memoirs* **174**, 331–346.
- Barnes, C. G., Petersen, S. W., Kistler, R. W., Prestvik, T. & Sundvoll, B. (1992). Tectonic implications of isotopic variation among Jurassic and Early Cretaceous plutons, Klamath Mountains. *Geological Society of America Bulletin* **104**, 117–126.
- Barnes, C. G., Johnson, K., Barnes, M. A., Prestvik, T., Kistler, R. W. & Sundvoll, B. (1995). The Grayback pluton: Magmatism in a Jurassic back-arc environment, Klamath Mountains, Oregon. *Journal of Petrology* **36**, 397–416.
- Barnes, C. G., Mars, E. V., Swapp, S. & Frost, C. D. (2006). Petrology and geochemistry of the Middle Jurassic Ironside Mountain Batholith: evolution of potassic magmas in a primitive arc setting. In: Snoke, A. W. & Barnes, C. G. (eds) *Geological Studies in the Klamath Mountains Province, California and Oregon: A Volume in Honor of William P. Irwin*. *Geological Society of America, Special Papers* **410**, 199–221.
- Barnes, C. G., Coint, N. & Yoshinobu, A. S. (2016a). Crystal accumulation in a tilted arc batholith. *American Mineralogist* **101**, 1719–1734. doi:10.2138/am-2015-5404.
- Barnes, C. G., Memeti, V. & Coint, N. (2016b). Deciphering magmatic processes in calc-alkaline plutons using trace element zoning in hornblende. *American Mineralogist* **101**, 328–342.
- Barnes, C. G., Werts, K., Memeti, V. & Ardill, K. (2019). Most granitoid rocks are cumulates: deductions from hornblende compositions and zircon saturation. *Journal of Petrology* **60**, 2227–2240.
- Bea, F., Montero, P. & Ortega, M. (2006). A LA-ICP-MS evaluation of Zr reservoirs in common crystal rocks: Implications for Zr and Hf geochemistry, and zircon-forming processes. *Canadian Mineralogist* **44**, 693–714.
- Bohrson, W. & Spera, F. (2001). Energy-constrained open-system magmatic processes II: Application of energy-constrained assimilation–fractional crystallization (EC-AFC) model to magmatic systems. *Journal of Petrology* **42**, 1019–1041.
- Bohrson, W. A. & Spera, F. J. (2007). Energy-constrained re-charge, assimilation, and fractional crystallization (EC-RA₂FC): a Visual Basic computer code for calculating trace element and isotope variations of open-system magmatic systems. *Geochemistry, Geophysics, Geosystems* **8**.
- Bucholz, C. E., Jagoutz, O., VanTongeren, J. A., Setera, J. & Wang, Z. (2017). Oxygen isotope trajectories of crystallizing melts: insights from modeling and the plutonic record. *Geochimica et Cosmochimica Acta* **207**, 154–184.
- Burgisser, A. & Bergantz, G. W. (2011). A rapid mechanism to remobilize and homogenize highly crystalline magma bodies. *Nature* **471**, 212–217.
- Claiborne, L. L., Miller, C. F., Walker, B. A., Wooden, J. L., Mazdab, F. K. & Bea, F. (2006). Tracking magmatic processes through Zr/Hf ratios in rocks and Hf and Ti zoning in zircons: An example from the Spirit Mountain batholith. *Mineralogical Magazine* **70**, 517–543.
- Coint, N., Barnes, C. G., Yoshinobu, A. S., Barnes, M. A. & Buck, S. (2013a). Use of trace element abundances in augite and hornblende to determine the size, connectivity, timing, and evolution of magma batches in a tilted pluton. *Geosphere* **9**, 1747–1765.
- Coint, N., Barnes, C. G., Yoshinobu, A. S., Chamberlain, K. R. & Barnes, M. A. (2013b). Batch-wise assembly and zoning of a tilted calc-alkaline batholith: field relations, timing, and compositional variation. *Geosphere* **9**, 1729–1746.
- Coleman, R. G., Manning, C. E., Mortimer, N., Donato, M. M. & Hill, L. B. (1988). Tectonic and regional metamorphic framework of the Klamath Mountains and adjacent Coast Ranges, California and Oregon. In: Ernst, W. G. (ed.) *Metamorphism and Crustal Evolution of the Western United States*. *Rubey Volume 7*. Englewood Cliffs, NJ: Prentice-Hall, pp. 1061–1097.
- Corfu, F., Hanchar, J. M., Hoskin, P. W. O. & Kinny, P. (2003). Atlas of zircon textures. In: Hanchar, J.M. & Hoskin, P.W.O. (eds.) *Zircon*. *Mineralogical Society of America and Geochemical Society, Reviews in Mineralogy and Geochemistry* **53**, 469–500.
- Dailey, S. R., Barnes, C. G., Leib, S. E. & Schoene, B. (2019). Evidence for the initiation of the Nevadan orogeny from partial melting of Rattlesnake Creek amphibolite, Klamath Mountains. *Geological Society of America, Abstracts with Programs* **51**, 214–215. doi:10.1130/abs/2019AM-336495.
- DePaolo, D. J. (1981). A neodymium and strontium isotopic study of the Mesozoic calc-alkaline granitic batholiths of the Sierra Nevada and Peninsular Ranges, California. *Journal of Geophysical Research* **86**, 10470–10488.
- Donato, M. M. (1989). Metamorphism of an ophiolitic tectonic mélange, northern California Klamath Mountains, USA. *Journal of Metamorphic Geology* **7**, 515–528.
- Donato, M. M., Barnes, C. G. & Tomlinson, S. L. (1996). The enigmatic Applegate Group of southwestern Oregon: Age, correlation, and tectonic affinity. *Oregon Geology* **58**, 79–91.
- Ernst, W. (1998). Geology of the Sawyers Bar Area, Klamath Mountains, Northern California. Map Sheet **47**, scale 1:

- 48,000, accompanying text 59 pp. California Division of Mines and Geology, Sacramento.
- Ernst, W. (1999). Mesozoic petro-tectonic development of the Sawyers Bar suprasubduction-zone arc, central Klamath Mountains, northern California. *Geological Society of America Bulletin* **111**, 1217–1232.
- Ernst, W. & Liu, J. (1998). Experimental phase-equilibrium study of Al- and Ti-contents of calcic amphibole in MORB—A semiquantitative thermobarometer. *American Mineralogist* **83**, 952–969.
- Ernst, W. G. (1990). Accretionary terrane in the Sawyers Bar area of the Western Triassic and Paleozoic Belt, central Klamath Mountains, northern California. In: Harwood, D.S. & Miller, M.M. (eds.) *Paleozoic and Early Mesozoic paleogeographic relations; Sierra Nevada, Klamath Mountains, and related terranes. Geological Society of America, Special Paper* **255**, 297–306.
- Ernst, W. G., Snow, C. A. & Scherer, H. H. (2008). Contrasting early and late Mesozoic petro-tectonic evolution of northern California. *Geological Society of America Bulletin* **120**, 179–194.
- Ernst, W. G., Wu, C., Lai, M. & Zhang, X. (2017). U–Pb ages and sedimentary provenance of detrital zircons from Eastern Hayfork meta-argillites, Sawyers Bar area, northwestern California. *Journal of Geology* **125**, 33–44.
- Frost, B. R., Barnes, C. G., Collins, W. J., Arculus, R. J., Ellis, D. J. & Frost, C. D. (2001). A geochemical classification for granitic rocks. *Journal of Petrology* **42**, 2033–2048.
- Frost, C. D., Barnes, C. G. & Snoko, A. W. (2006). Nd and Sr isotopic data from argillaceous rocks of the Galice Formation and Rattlesnake Creek terrane, Klamath Mountains: evidence for the input of Precambrian sources. In: Snoko, A. W. & Barnes, C. G. (eds) *Geological Studies in the Klamath Mountains Province, California and Oregon: A Volume in Honor of William P. Irwin. Geological Society of America, Special Papers* **410**, 103–120.
- Garlick, S. R., Medaris, L. G., Jr, Snoko, A. W., Schwartz, J. J. & Swapp, S. M. (2009). Granulite- to amphibolite-facies metamorphism and penetrative deformation in a disrupted ophiolite, Klamath Mountains, California: a deep view into the basement of an accreted oceanic arc. In: Miller, R. B. & Snoko, A. W. (eds) *Crustal Cross Sections from the Western North American Cordillera and Elsewhere: Implications for Tectonic and Petrologic Processes. Geological Society of America, Special Papers* **456**, 151–186.
- Gordon, S. M., Miller, R. B. & Sauer, K. B. (2017). Incorporation of sedimentary rocks into the deep levels of continental magmatic arcs: links between the North Cascades arc and surrounding sedimentary terranes. In: Haugerud, R. A. & Kelsey, H. M. (eds) *From the Puget Lowland to East of the Cascade Range. Geologic Excursions in the Pacific Northwest* **49**, 101–141.
- Gray, G. G. (1986). Native terranes of the central Klamath Mountains. *Tectonics* **5**, 1043–1054.
- Grunder, A. L. (1992). Two-stage contamination during crustal assimilation: isotopic evidence from volcanic rocks in eastern Nevada. *Contributions to Mineralogy and Petrology* **112**, 219–229.
- Hacker, B. R., Donato, M. M., Barnes, C. G., McWilliams, M. O. & Ernst, W. G. (1995). Timescales of orogeny: Jurassic construction of the Klamath Mountains. *Tectonics* **14**, 677–703.
- Hildreth, W. (2004). Volcanological perspectives on Long Valley, Mammoth Mountain, and Mono Craters: several contiguous but discrete systems. *Journal of Volcanology and Geothermal Research* **136**, 169–198.
- Hildreth, W. & Moorbath, S. (1988). Crustal contributions to arc magmatism in the Andes of central Chile. *Contributions to Mineralogy and Petrology* **98**, 455–489.
- Holness, M. B. & Sawyer, E. W. (2008). On the pseudomorphing of melt-filled pores during the crystallization of migmatites. *Journal of Petrology* **49**, 1343–1363.
- Humphreys, M. C. S., Blundy, J. D. & Sparks, R. S. (2006). Magma evolution and open-system processes at Shiveluch Volcano: insights from phenocrysts zoning. *Journal of Petrology* **47**, 2303–2334.
- Humphreys, M. C. S., Christopher, T. & Hards, V. (2009). Microlite transfer by disaggregation of mafic inclusions following magma mixing at Soufrière Hills volcano. *Contributions to Mineralogy and Petrology* **157**, 609–624.
- Irwin, W. P. (1972). Terranes of the Western Paleozoic and Triassic belt in the southern Klamath Mountains, California. *US Geological Survey Professional Papers* **800-C**, 103–111.
- Irwin, W. P. (1981). Tectonic accretion of the Klamath Mountains. In: Ernst, W. G. (ed.) *The Geotectonic Development of California; Rubey Volume I*. Englewood Cliffs, NJ: Prentice–Hall, pp. 29–49.
- Jachens, R. C., Barnes, C. G. & Donato, M. M. (1986). Subsurface configuration of the Orleans fault: implications for deformation in the western Klamath Mountains. *Geological Society of America Bulletin* **97**, 388–395.
- Jagoutz, O. & Klein, B. (2018). On the importance of crystallization–differentiation for the generation of SiO₂-rich melts and the compositional build-up of arc (and continental) crust. *American Journal of Science* **318**, 29–63.
- Jagoutz, O., Müntener, O., Ulmer, P., Pettke, T., Burg, J.-P., Dawood, H. & Hussain, S. (2007). Petrology and mineral chemistry of lower crustal intrusions: the Chilas Complex, Kohistan (NW Pakistan). *Journal of Petrology* **48**, 1895–1953.
- Jagoutz, O. E., Burg, J.-P., Hussain, S. S., Dawood, H., Pettke, T., Iizuka, T. & Maruyama, S. (2009). Construction of the granulite crust of an island arc part I: geochronological and geochemical constraints from the plutonic Kohistan (NW Pakistan). *Contributions to Mineralogy and Petrology* **158**, 739–755.
- Karakas, O., Wotzlaw, J. F., Guillong, M., Ulmer, P., Brack, P., Economos, R., Bergantz, G. W., Sinigoi, S. & Bachmann, O. (2019). The pace of crustal-scale magma accretion and differentiation beneath silicic caldera volcanoes. *Geology* **47**, 719–723.
- Klein, B. Z. & Jagoutz, O. (2021). Construction of a trans-crustal magma system: building the Bear Valley Intrusive Suite, southern Sierra Nevada, California. *Earth and Planetary Science Letters* **553**, 116624. doi:10.1016/j.epsl.2020.116625.
- Klein, B. Z., Jagoutz, O. & Ramezani, J. (2021). High-precision geochronology requires that ultrafast mantle-derived magmatic fluxes built the transcrustal Bear Valley Intrusive Suite, Sierra Nevada, California, USA. *Geology* **49**, 106–110. doi:10.1130/G47952.1.
- Kita, N. T., Ushikubo, T., Fu, B. & Valley, J. W. (2009). High precision SIMS oxygen isotope analysis and the effect of sample topography. *Chemical Geology* **264**, 43–57.
- Krogh, T. E. (1973). A low contamination method for hydrothermal decomposition of zircon and extraction of U and Pb for isotopic age determinations. *Geochimica et Cosmochimica Acta* **37**, 485–494.
- Lackey, J. S., Valley, J. W. & Saleeby, J. B. (2005). Supracrustal input to magmas in the deep crust of Sierra Nevada batholith: evidence from high- $\delta^{18}\text{O}$ zircon. *Earth and Planetary Science Letters* **235**, 315–330.

- Lackey, J. S., Valley, J. W., Chen, J. H. & Stockli, D. F. (2008). Dynamic magma systems, crustal recycling, and alteration in the central Sierra Nevada batholith: the oxygen isotope record. *Journal of Petrology* **49**, 1397–1426.
- Lanphere, M. A., Irwin, W. P. & Hotz, P. E. (1968). Isotopic age of the Nevadan Orogeny and older plutonic and metamorphic events in the Klamath Mountains, California. *Geological Society of America Bulletin* **79**, 1027–1052.
- Leib, S. E., Hetherington, C. J. & Yoshinobu, A. S. (2020). Rotated prograde garnet with rutile demonstrate high-grade Nevadan metamorphism in overly thickened continental crust in the central Klamath Mountains. *Geological Society of America, Abstracts with Programs* **52**, 201–210. doi: 10.1130/abs/2020AM-358248.
- Ludwig, K. R. (1988). PBDAT for MS-DOS, a computer program for IBM-PC compatibles for processing raw Pb-U-Th isotope data, version 1.24: U.S. Geological Survey, Open-File Report 88-542, 32 pp.
- Ludwig, K. R. (1991). PbDAT for MS-DOS: a computer program for IBM-PC compatibles for processing raw Pb-U-Th isotope data, version 1.20. U.S. Geological Survey, Open File Report, 88-542, 34 pp.
- Ludwig, K. R. (1998). On the treatment of concordant uranium–lead ages. *Geochimica et Cosmochimica Acta* **62**, 665–676.
- Mattinson, J. M. (2005). Zircon U–Pb chemical abrasion (“CA-TIMS”) method: combined annealing and multi-step partial dissolution analysis for improved precision and accuracy of zircon ages. *Chemical Geology* **220**, 47–66.
- Matzel, J. E. P., Bowring, S. A. & Miller, R. B. (2006). Time scales of pluton construction at differing crustal levels: examples from the Mount Stuart and Tenpeak intrusions, North Cascades, Washington. *Geological Society of America Bulletin* **118**, 1412–1430.
- Mazdab, F. M. & Wooden, J. L. (2006). Trace element analysis in zircon by ion microprobe (SHRIMP-RG); technique and applications. *Geochimica et Cosmochimica Acta* **70**, A405.
- McBirney, A. R., Taylor, H. P. & Armstrong, R. L. (1987). Paricutin re-examined: a classic example of crustal assimilation in calcalkaline magma. *Contributions to Mineralogy and Petrology* **95**, 4–20.
- Miller, J. S., Matzel, J. E. P., Miller, C. F., Burgess, S. D. & Miller, R. B. (2007). Zircon growth and recycling during the assembly of large composite arc plutons. *Journal of Volcanology and Geothermal Research* **167**, 282–299.
- Mortimer, N. & Coleman, R. G. (1985). A Neogene structural dome in the Klamath Mountains, California and Oregon. *Geology* **13**, 253–256.
- Otamendi, J. E., Ducea, M. N., Tibaldi, A. M., Bergantz, G. W., De La Rosa, J. D. & Vujovich, G. I. (2009). Generation of tonalitic and dioritic magmas by coupled partial melting of gabbroic and metasedimentary rocks within the deep crust of the Famatinian magmatic arc. *Journal of Petrology* **50**, 841–873.
- Otamendi, J. E., Ducea, M. N. & Bergantz, G. W. (2012). Geological, petrological and geochemical evidence for progressive construction of an arc crustal section, Sierra de Valle Fértil, Famatinian arc, Argentina. *Journal of Petrology* **53**, 761–800.
- Otten, M. T. (1984). The origin of brown hornblende in the Artfjället gabbro and dolerites. *Contributions to Mineralogy and Petrology* **86**, 189–199.
- Parrish, R. R., Roddick, J. C., Loveridge, W. D. & Sullivan, R. W. (1987). Uranium-lead analytical techniques at the Geochronology Laboratory, Geological Survey of Canada. *In Radiogenic age and isotopic studies: Geological Survey of Canada Paper* **87-2**, 3–7.
- Paterson, S., Memeti, V., Mundil, R. & Žák, J. (2016). Repeated, multiscale, magmatic erosion and recycling in an upper-crustal pluton: Implications for magma chamber dynamics and magma volume estimates. *American Mineralogist* **101**, 2176–2198.
- Pe-Piper, G. (1988). Calcic amphiboles of mafic rocks of the Jeffers Brook plutonic complex, Nova Scotia, Canada. *American Mineralogist* **73**, 993–1006.
- Perugini, D. & Poli, G. (2004). Analysis and numerical simulation of chaotic advection and chemical diffusion during magma mixing: petrological implications. *Lithos* **78**, 43–66.
- Perugini, D., Petrelli, M. & Poli, G. (2006). Diffusive fractionation of trace elements by chaotic mixing of magmas. *Earth and Planetary Science Letters* **243**, 669–680.
- Perugini, D., De Campos, C. P., Dingwell, D. B., Petrelli, M. & Poli, G. (2008). Trace element mobility during magma mixing: preliminary experimental results. *Chemical Geology* **256**, 146–157.
- Pickett, D. A. & Saleeby, J. B. (1993). Thermobarometric constraints on the depth of exposure and conditions of plutonism and metamorphism at deep levels of the Sierra Nevada batholith, Tehachapi Mountains. *Journal of Geophysical Research: Solid Earth* **98**, 609–629.
- Pickett, D. A. & Saleeby, J. B. (1994). Nd, Sr, and Pb isotopic characteristics of Cretaceous intrusive rocks from deep levels of the Sierra Nevada batholith, Tehachapi Mountains, California. *Contributions to Mineralogy and Petrology* **118**, 198–215.
- Putirka, K. (2016). Amphibole thermometers and barometers for igneous system, and some implications for eruption mechanisms of felsic magmas at arc volcanoes. *American Mineralogist* **101**, 841–858.
- Richard, P., Shimizu, N. & Allègre, C. J. (1976). $^{143}\text{Nd}/^{144}\text{Nd}$, a natural tracer: an application to oceanic basalts. *Earth and Planetary Science Letters* **31**, 269–278.
- Ruprecht, P., Bergantz, G. W., Cooper, K. M. & Hildreth, W. (2012). The crustal magma storage system of Volcán Quizapu, Chile, and the effects of magma mixing on magma diversity. *Journal of Petrology* **53**, 801–840.
- Sawyer, E. (1999). Criteria for the recognition of partial melting. *Physics and Chemistry of Earth (A)* **24**, 269–279.
- Schärer, U. (1984). The effect of initial ^{230}Th disequilibrium on young U–Pb ages: The Makalu case, Himalaya. *Earth and Planetary Science Letters* **67**, 191–204, doi: 10.1016/0012-821X(84)90114-6.
- Schmidt, M. E. & Grunder, A. L. (2011). Deep mafic roots to arc volcanoes: mafic recharge and differentiation of basaltic andesite at North Sister volcano, Oregon Cascades. *Journal of Petrology* **52**, 603–641.
- Singer, B. S., Smith, K. E., Jicha, B. R., Beard, B. L., Johnson, C. M. & Rogers, N. W. (2011). Tracking open-system differentiation during growth of Santa María Volcano, Guatemala. *Journal of Petrology* **52**, 2335–2363.
- Sinigoï, S., Quick, J. E., Demarchi, G. & Klötzli, U. S. (2016). Production of hybrid granitic magma at the advancing front of basaltic underplating: Inferences from the Sesia Magmatic System (south-western Alps, Italy). *Lithos* **252–253**, 109–122.
- Snoke, A. W. & Barnes, C. G. (2006). The development of tectonic concepts for the Klamath Mountains Province, California and Oregon. In: Snoke, A. W. & Barnes, C. G. (eds) *Geological Studies in the Klamath Mountains Province, California and Oregon: A Volume in Honor of William P. Irwin: Geological Society of America, Special Papers* **410**, 1–29. doi:10.1130/2006.2410(01).
- Solano, J. M. S., Jackson, M. D., Sparks, R. S. J., Blundy, J. D. & Annen, C. (2012). Melt segregation in deep crustal hot zones: a mechanism for chemical differentiation, crustal assimilation and the formation of evolved magmas. *Journal of Petrology* **53**, 1999–2026.

- Spera, F. & Bohron, W. (2001). Energy-constrained open-system magmatic processes I: general model and energy-constrained assimilation and fractional crystallization (EC-AFC) formulation. *Journal of Petrology* **42**, 999–1018.
- Spera, F. J. & Bohron, W. A. (2018). Rejuvenation of crystal magma mush: a tale of multiply nested processes and time-scales. *American Journal of Science* **318**, 90–140.
- Steiger, R. H. & Jäger, E. (1977). Subcommittee on geochronology: Convention on the use of decay constants in geo- and cosmochronology. *Earth and Planetary Science Letters* **36**, 356–362.
- Tibaldi, A. M., Otamendi, J. E., Cristofolini, E. A., Baliani, I., Walker, B. A. & Bergantz, G. W. (2013). Reconstruction of the Early Ordovician Famatinian arc through thermobarometry in lower and middle crustal exposures, Sierra de Valle Fértil. *Tectonophysics* **589**, 151–166.
- Valley, J. W. (2003). Oxygen isotopes in zircon. In: Hanchar, J. M. & Hoskin, P. W. O. (eds) *Mineralogical Society of America, Reviews of Mineralogy and Geochemistry* **53**, 343–385.
- Valley, J. W. & Kita, N. T. (2009). *In situ* oxygen isotope geochemistry by ion microprobe. In: Fayek, M. (ed.) *Secondary ion mass spectrometry in the earth sciences: Gleaning the big picture from a small spot. Mineralogical Association of Canada, Short Course Series* **41**, 19–63.
- Vervoort, J. D. & Blichert-Toft, J. (1999). Evolution of the depleted mantle: Hf isotope evidence from juvenile rocks through time. *Geochimica et Cosmochimica Acta* **63**, 533–556.
- Wagner, D. L. & Saucedo, G. J. (1987). *Geologic map of the Weed Quadrangle, 4 sheets, 1:250,000*. California Division of Mines and Geology, San Francisco.
- Walker, B. A., Jr, Bergantz, G. W., Otamendi, J. E., Ducea, M. N. & Cristofolini, E. A. (2015). A MASH zone revealed: the mafic complex of the Sierra Valle Fértil. *Journal of Petrology* **56**, 1863–1896.
- Wang, X.-L., Coble, M. A., Valley, J. W., Shu, X.-J., Kitajima, K., Spicuzza, M. J. & Sun, T. (2014). Influence of radiation damage on late Jurassic zircon from southern China: evidence from *in situ* measurement of oxygen isotopes, laser Raman, U–Pb ages, and trace elements. *Chemical Geology* **389**, 122–136.
- Whitney, D. L. & Evans, B. W. (2010). Abbreviations for names of rock-forming minerals. *American Mineralogist* **95**, 185–187.
- Wright, J. E. (1982). Permo-Triassic accretionary subduction complex, southwestern Klamath Mountains. *Journal of Geophysical Research* **87**, 3805–3818.
- Wright, J. E. & Fahan, M. R. (1988). An expanded view of Jurassic orogenesis in the western United States Cordillera: Middle Jurassic (pre-Nevadan) regional metamorphism and thrust faulting within an active arc environment, Klamath Mountains, California. *Geological Society of America Bulletin* **100**, 859–876.
- Wright, J. E. & Wyld, S. J. (1994). The Rattlesnake Creek terrane, Klamath Mountains, California: an early Mesozoic volcanic arc and its basement of tectonically disrupted oceanic crust. *Geological Society of America Bulletin* **106**, 1033–1056.
- Zhang, Y. & Ni, H. (2010). Diffusion of H, C, and O components in silicate melts. In: Zhang, Y. & Cherniak, D. J. (eds) *Diffusion in minerals and melts. Mineralogical Society of America and Geochemical Society, Reviews in Mineralogy and Geochemistry* **72**, 171–225.